

European Wind Energy Master – EWEM – Rotor Design Track

**Department of
Wind Energy
DTU**

Master Project

Design Requirements for 2-D Aero-elastic Experiments on Aerofoils

Eyob Berhanu Gashaw

Student number (s122601/ 4260805)

July, 2014

DTU Vindenergi
Institut for Vindenergi



**Department of Aerospace
Engineering TU Delft**



Danmarks Tekniske Universitet

DTU Vindenergi
Nils Koppels Allé
Bygning 403
2800 Kgs. Lyngby

Delft University of Technology

Faculty of Aerospace Engineering,
TU Delft
Kluyverweg 1, 2629 HS Delft
the Netherlands

Copyright © Eyob Berhanu Gashaw, 2014

Printed in Denmark, Lyngby

Authors: Eyob Berhanu Gashaw

Title: Design Requirements for 2-D Aero-elastic Experiments
on Airfoils

Department: Wind Energy at Technical University of Denmark and
Aerospace Engineering at Delft University of Technology

Abstract:

Given the prime importance of wind tunnel setup when it comes to aero-elastic study, the main intent of this project is to devise a mechanism for supporting system of 2D aero-elasticity experiment in the Red Wind Tunnel Facility at DTU that allows three-degree-of-freedom motion of the rigid model. This project work is mainly inspired by the fact that deep stall aero-elastic Characteristics of wind turbines, which govern the design of stall-regulated wind turbines at high wind speed, have been barely investigated in literatures so far. So in redesigning the test section of the wind tunnel facility the following sub-tasks are included: (1) Literature survey on test section design/construction for 2D aero-elastics testing of aerofoils. (2) Panel code simulation of wing/tunnel interaction. (3) Adapted design of new test section to the Red wind tunnel facility. (4) To some extent building and testing the new test section. The implementation and actual design may be too time demanding to be fulfilled within the given time slot, however a specific design for the Red tunnel facility is documented through flow analysis and drawings at the end of the project. Among which the first and third item have been addressed and the fourth item partially as well, but the second item is still to be done with the flow solver Q³UIC which was developed by Néstor in DTU. Since the aerodynamic code of this tool is only for pitching motion, extending this tool for this thesis work happened to be out of scope.

July, 2014

Project Period:

[2014.02.03 – 2014.07.24]

ECTS:

[30]

Education:

Master of Science

Field:

Wind Energy and Aerospace Engineering

Supervisors:

Martin O. L. Hansen, Robert F.
Mikkelsen, Nando Timmer

Remarks:

This report is submitted as partial fulfillment of the requirements for graduation in the above education at the Technical University of Denmark and Delft University of Technology.

Project no.:

[Text]

Cover: Master Report

Pages: 49

Tables: 3

References: 27

Danmarks Tekniske Universitet

DTU Vindenergi
Nils Koppels Allé
Bygning 403
2800 Kgs. Lyngby
Phone (+45) 45 25 25 25
www.vindenergi.dtu.dk

Delft University of Technology

Faculty of Aerospace Engineering,
TU Delft
Kluyverweg 1, 2629 HS Delft
the Netherlands
Phone +31 15 2786388

www.lr.tudelft.nl

Preface

The undersigned hereby certify that they have read and recommend to the European Wind Energy Master – EWEM for acceptance of a thesis entitled “**Design Requirements for 2D Aeroelastic Experiments on Airfoils**” by **Eyob Berhanu Gashaw** in partial fulfilment of the requirements for the degree of **Master of Science**.

Dated: July 24, 2014

Supervisor:

Martin O. L. Hansen, Denmark Technical University

Supervisor:

Robert F. Mikkelsen, Denmark Technical University

Supervisor:

Nando Timmer, Delft University of Technology

Content

1.	Introduction.....	1
2.	Literature survey on test section design/construction.....	3
2.1	Low damping mount system.....	3
2.2	Multiparameter Mount system.....	5
2.3	Mount system for testing structural nonlinearities.....	6
2.4	Free and forced excitation mechanism.....	8
2.5	Conclusion.....	10
3.	Theory.....	10
3.1	Induced velocities due to elastic deformations.....	10
3.2	Governing Equations of motion.....	11
4.	Experimental Set-up.....	14
4.1	Mount system Overview.....	14
4.2	Frame.....	15
4.3	Pitch module.....	17
4.3.1	Torsional stiffness.....	20
4.4	Plunging and lead-lag module.....	21
5.	Analytical Results, Outcome and Relevance.....	24
5.1	Dynamic stall model (DSM).....	25
5.1.1	Response of system for $\alpha g = 0^\circ$	26
5.1.2	Response of system for $\alpha g = 15^\circ$	26
5.2	Direction of vibration.....	27
5.3	Aerodynamic damping vs. direction of vibration.....	28
6.	Summary.....	30
7.	References.....	31
8.	Appendix.....	32
8.1	Stiffness.....	32
8.2	Aerodynamic damping.....	33
8.3	Different views of the mount system.....	35
8.4	Masses of parts.....	42
9.	Acknowledgements.....	43

1. Introduction

Aero-elasticity is a field of study which deals with the interaction of structural, inertial and aerodynamic forces and the importance of its knowledge becomes quite indispensable in connection with capturing more of the wind energy with large MW offshore and onshore wind turbines as their blades become more flexible proportional to blade length.^[8] Associated with such turbines, there are two main aero-elastic instability problems known as stall-induced vibration (stall flutter) and classical flutter which are linked to the two major types of current commercial wind turbines - stall-regulated and pitch-regulated – respectively.^[15] Stall-regulated turbines are operating with their flow either partially or fully separated and hence experience stall-induced vibration in connection with the non-linear interaction between aerodynamic load and blade structural flexibility. This kind of instability is not an issue for pitch-regulated wind turbines unless they are parking or operating close to stall for high performance. Rather, classical flutter is usually the case for this type of wind turbines which is due to coupling of the flap-wise and torsional modes of vibration with a flutter oscillation frequency of between the two involving structural modes, unlike stall flutter which usually involves only one structural mode.^[1, 15] The risk of stall-induced vibrations is mainly related to blade aerofoil characteristics that give rise to negative aerodynamic damping which may be greater than the structural damping of the blade depending on the effective direction of blade vibration, as shown in [Figure 1](#), relative to rotor plane in which case increasing the structural damping may be an option.^[15]

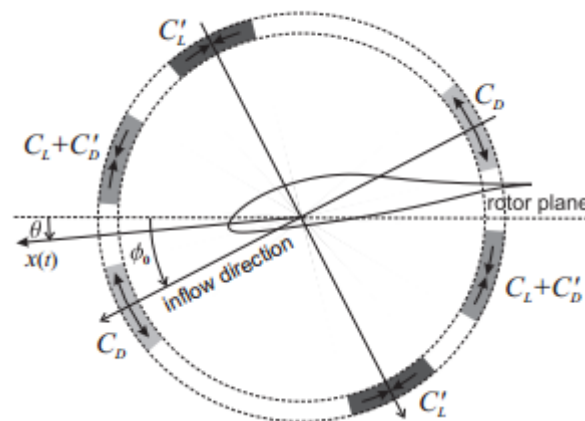


Figure 1 Important ranges of directions of vibration relative to the inflow direction given by the aerodynamic damping coefficient ^[15]

Dealing with such stall behaviour with quasi-steady aerodynamic analysis can be misleading as it underestimates the performance with the use of static measurement data in wind tunnels for the aerofoil characteristics^[21] and hence different dynamic stall models have been developed by different scientists so far related to study of unsteady aerodynamics which is still a current area of research.^[16-17] Dynamic stall model may be used to determine the performance of rotor blades if the aerofoil is operating in stalled flow, but not fully separated. However, if the flow is fully separated which is referred to as deep stall, the aerofoil characteristics are victims of large uncertainty.^[15] This is the main motivation behind upgrading the Red Wind Tunnel Facility at DTU

while the fact that the deep stall aerofoil characteristics result in negative aerodynamic damping of blades greater than structural damping only when vibrating in certain directions relative to the rotor plane is the main inspiration to synthesize the mount system for the aerofoil model that allows three Degree-Of-Freedom (DOF) motion – edgewise, plunging, and pitching – to be implemented in the wind tunnel test section. The three DOF is in fact what makes the mount system different from previous studies of same sort so far that consider only heaving and pitching motions.^[1-7] The notion of this thesis work is largely based on the paper *Aeroelastic instability problems for wind turbines* by M. H. Hansen in 2007. ^[15] The support mechanism is designed so as to allow free oscillations and also independent motion of each DOF.

This thesis work is kind of a documentation of the mount system design. Accordingly a review of relevant previous studies related to the present work under study in connection with what to be adapted and added to this project work was carried out and it is presented in the next section. Then the detail design of the new mount system is explained. This is followed by theoretical modelling of the aeroelasticity for the system under study and a description of the methodology in developing the design of the wind tunnel test section, which involves coupling the aerodynamic flow solver with the aeroelasticity equation.

2. Literature survey on test section design/construction

Aeroelasticity experiments for testing the various aero-elastic instabilities like divergence (static) and flutter (dynamic) have been carried out starting from the Wright brothers in 1899.^[9] Depending on the application area the tests were being conducted with different mounting systems for the airfoil model. For instance, flexible semi-span models mounted on the sidewall of the wind tunnel as a cantilever beam ^[10-11], full-span models mounted on a cable system ^[12-14]. On the contrary, rigid wing models on a flexible mounting system were also used ^[1-5]. In the following sections the findings of few of the most relevant previous studies are reviewed, more of the latter types. This is followed by some drawn conclusions out of the literature survey.

All the experimental supporting systems discussed in this section are based on the well-known theoretical 2D aero-elastic model shown in Figure 2. Where k_y and k_α are the plunging and pitching stiffness corresponding to the two-degrees-of-freedom plunging y and pitching α respectively, the aerodynamic loads lift and moment L & M , mass m , wind speed V and center of mass at a distance r from elastic axis.

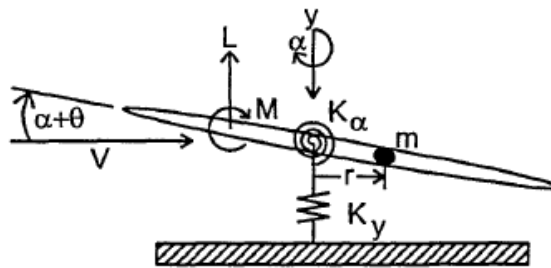


Figure 2 2D aero-elastic model ^[7]

2.1 Low damping mount system

The simplest experimental set up for 2D aero-elastic experiment is the one by Mosses G. Farmer in 1982. ^[1] What makes this two-degree-of-freedom mount system outstanding compared to those adopted until then is that it can only introduce small damping which does not change when the load on the model changes and hence the only damping in the system is aerodynamic damping. This is because it does not use bearings in the mount system as they introduce damping by their own which changes when the load on the model changes. As shown in Figure 5 and Figure 7 the rigid model is attached to a splitter plate so that the two move together as one rigid mass. The splitter plate is attached to a turntable by using four circular rods of same diameter D which are screwed to both symmetrically in a way they can form a fixed-fixed end condition. This ensures that the splitter plate can only move when the rods deform elastically. The wind-off characteristics of the mount system are determined from the rods, drag strut which provides edgewise stiffening, and mass of splitter plate and rigid model.

The rods provide plunging stiffness with their bending constant (EI) as a cantilever beam as shown in Figure 3. From simple beam theory the stiffness is defined as load per unit deflection in

the direction of the load and hence the equivalent stiffness for the four identical rods in parallel can be written as in equation (2.1).

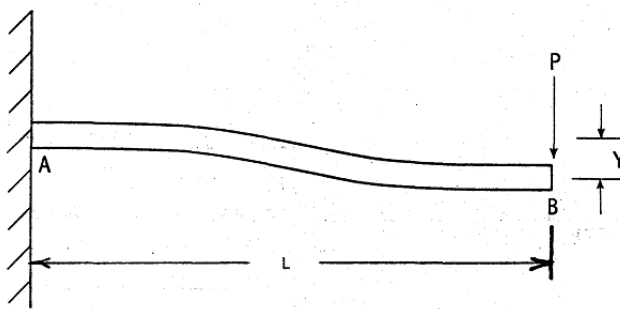


Figure 3 Schematic drawing of beam deflection [1]

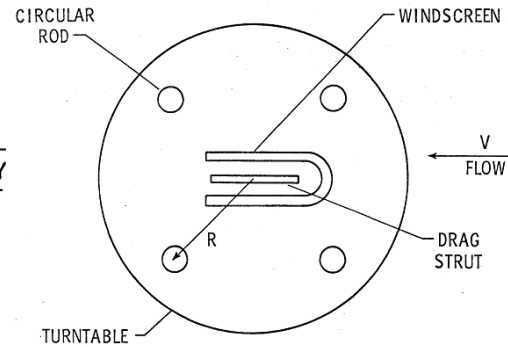


Figure 4 Horizontal view looking perpendicular to the face of the turntable [1]

$$k_p = 4 \frac{P}{y} = 4 \times \frac{12EI}{L^3} = \frac{48EI}{L^3} \quad (2.1)$$

Where y is the vertical deflection, P is the perpendicular load, and $I = \frac{\pi D^4}{64}$, L , E , are moment of inertia, length, and Young's modulus of each rod respectively. The pitch stiffness is derived from both twisting and bending of the rods. The twisting in each rod by θ induces a bending deflection of $R\theta$ on each rod as well, which is equivalent to a torque of $4 \frac{P}{y} R\theta \times R = 4 \frac{P}{y} R^2\theta$. So, together with the torsional stiffness contribution from the strut, the total pitching stiffness can be computed as in equation (2.2) with $J = \frac{\pi D^4}{32}$ as polar moment of inertia of each rod.

$$k_\theta = 4 \left(\frac{T}{\theta} + \frac{P}{y} R^2 \right) = 4 \left(\frac{GJ}{L} + \frac{12EI}{L^3} R^2 \right) \quad (2.2)$$

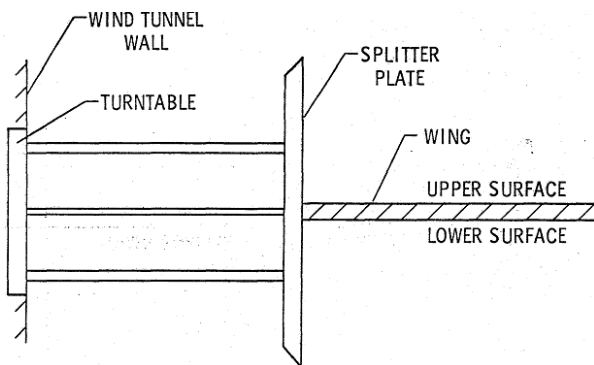


Figure 5 Horizontal view looking upstream (windscreen not shown) [1]

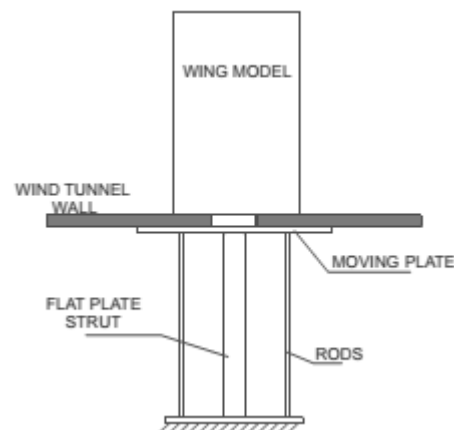


Figure 6 Side view of the flutter mount system, [3]

The windscreen shown in [Figure 4](#) is to shield the air flow over the strut, in addition to limiting excessive vibrations, so that it does not affect the aerodynamics of the rest of the system. For instance, somehow equivalent to the function of the windscreen, the entire flexible mount system can be kept away from the flow field as it was implemented in a wind tunnel with a test section of 2 m² by aligning the splitter plate with the wind tunnel wall as shown in [Figure 6](#).^[3]

This simple experimental setup was developed to do flutter test and its prototype was tested in a wind tunnel with a square test section of 16ft² and it was possible to find results matching to those found analytically and consistent with findings from other studies of same sort, but only free (spring supported) oscillation experiments can be carried out.



Figure 7 A wing installed on the mount system in the wind tunnel ^[1]

2.2 Multiparameter Mount system

A recent work by Gjerek, et al. ^[6] is a new concept that allows mounting different wing models and also varying the structural parameters of the aero-elastic system like stiffness. Besides, as shown in [Figure 9](#) the rigid wing model is mounted vertically as a workaround for the gravity effect on plunging and pitching motion, unlike the horizontal arrangement in ^[1], [Figure 7](#). As shown in the CAD model, [Figure 8](#), the pair of steel cantilever beams provide plunging stiffness which can be varied by changing the length. The pitch stiffness is provided by a disc with a pair of preloaded extension springs that can be adjusted by modifying disc size and spring characteristic. And the wing support axis defines the elastic axis and is supported by ball bearings at both ends. The system has a provision for forced excitation as well.

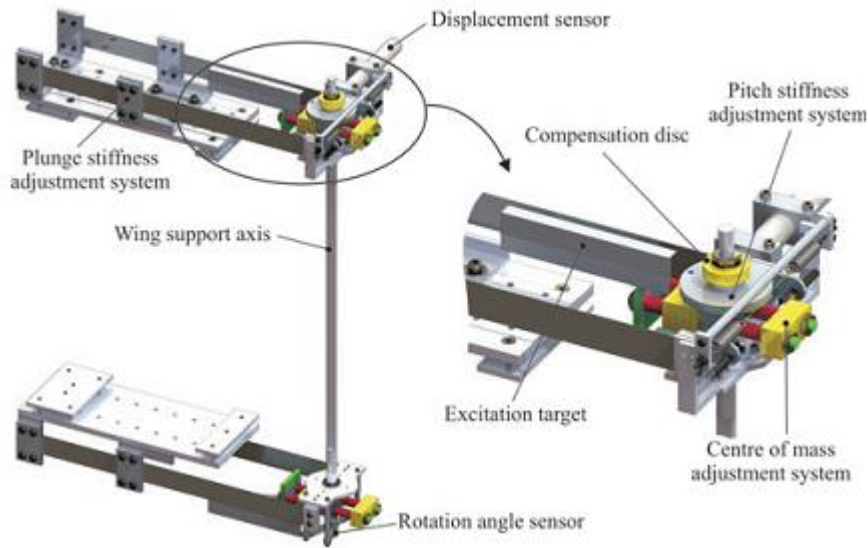


Figure 8 CAD model of the support system [6]

This experimental setup was successfully used to study the effect of airfoil thickness on the stability boundary of observed aero-elastic system as it allows changing the rigid wing model. Besides, the supporting system can be used to test flexible wing model and bridge deck sections.

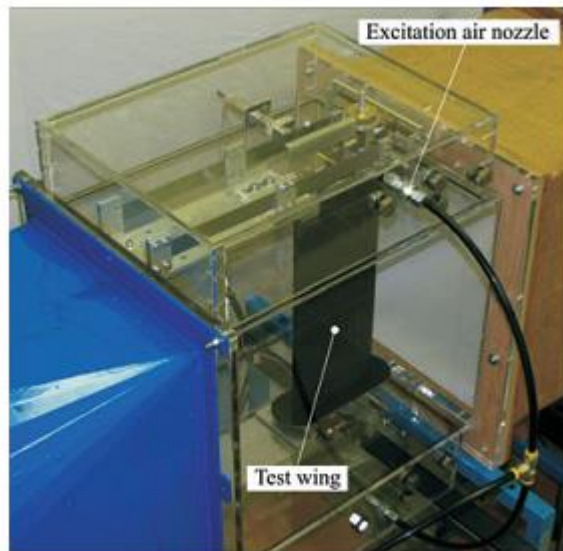


Figure 9 Test wing in the wind tunnel test section [6]

2.3 Mount system for testing structural nonlinearities

The mount system developed by O'Neil, et al. [7] was developed on the ground that the governing equations for Aeroelastic system describe both the structure and flow field and hence the nonlinearities can be introduced through the structural terms – like those involving stiffness and/or damping – and/or through the unsteady aerodynamic terms – like the unsteady airfoil

characteristics. To this end, they investigated prescribed nonlinear responses which are governed by a pair of cams employed with prescribed nonlinear shapes as shown in Figure 10 and Figure 11.

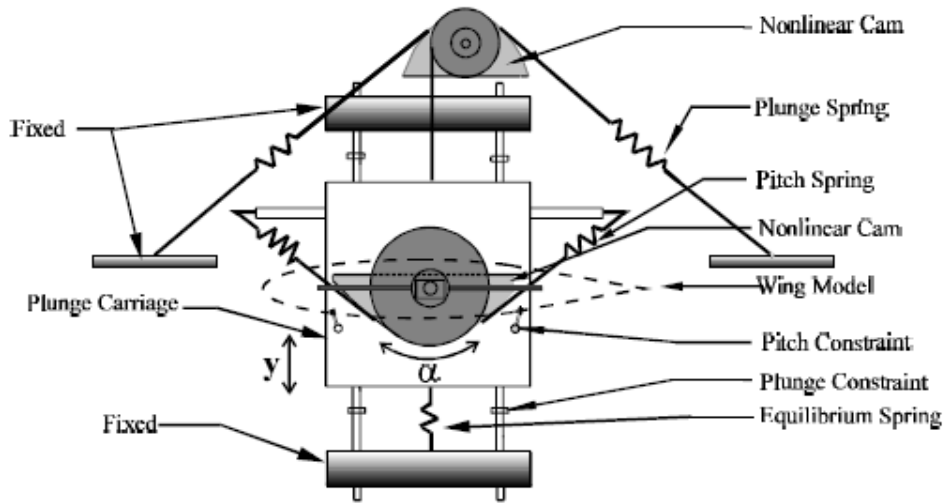


Figure 10 The model support system permits prescribed nonlinear motion in two degrees of freedom [7]

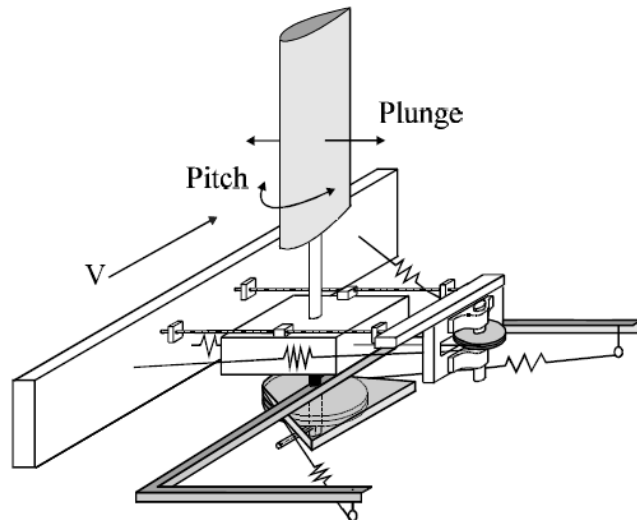


Figure 11 A second view of the model support system is shown [7]

The plunging motion is effected through a carriage mounted on rails with amplitude limiting constraints to avoid excessive vibration leading to the test apparatus damage. Whereas the pitching motion is governed by the bearings mounted on the same carriage. In the flutter analysis the mass of the carriage does not take part in calculating the mass moment of inertia as it does not involve in the pitching motion, but the total mass for the plunging motion comprises mass of the wing plus that of moving components of the supporting structure.

2.4 Free and forced excitation mechanism

Unlike the mount systems discussed above, the set up by Yogesh Babbar, et al. ^[2] in Figure 12 gives more control for the forced oscillation experiment. ^[2] On the paper published by the authors, ^[2] it is shown how to carry out forced oscillations of primarily the pitching motion, but the design has the capability of allowing forced plunging oscillations as well.

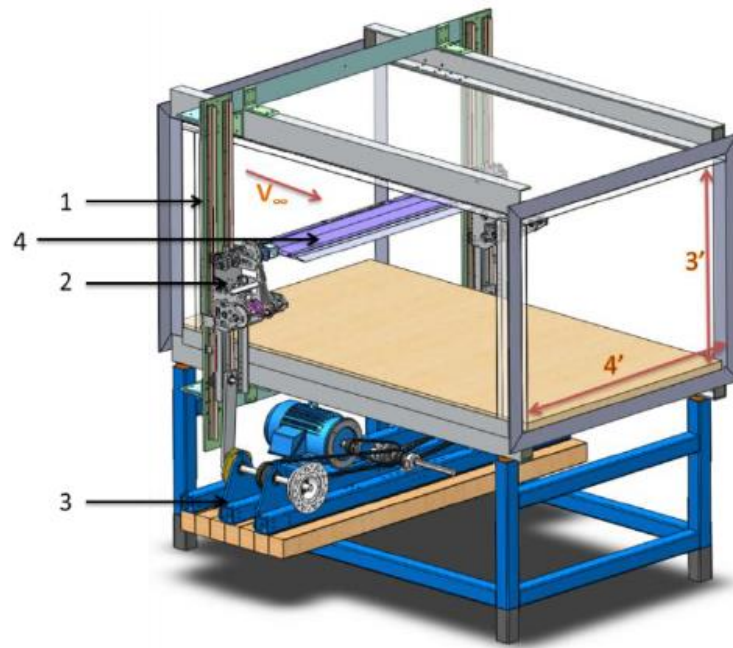


Figure 12 PPDS major subassemblies 1. Frame, 2. Pitch Module, 3. Plunge Mechanism, 4. Wing Balance subassembly ^[2]

It has a pair of pitching mechanisms on both ends of the rigid wing model, which runs from wall to wall of the wind tunnel test section, for generating and measuring the pitch motion. Each pitch module entails identical slider crank mechanism and driving servo motor which are part of the plunging mechanism on each side of the test section which by itself involves another four bar mechanism to generate the plunging motion. So the single motor at the bottom for the plunging mechanism drives all moving components of the mounting system and model as a single payload. On the other hand, The pitching and plunging mechanisms at one side in (See Figure 13 and Figure 14) are driven independently by their own servo motors and the former is connected to the latter through the connecting rod of the plunging four bar mechanism. So these two mechanisms provide independent forced excitation of the plunging and pitching motion or a combined synchronized excitation of the two-degree-of-freedom motions. The plunge motor drive is split into the two drive shafts on either side of the test section by using belts. For further details of design and manufacturing of the experimental setup refer ^[2].

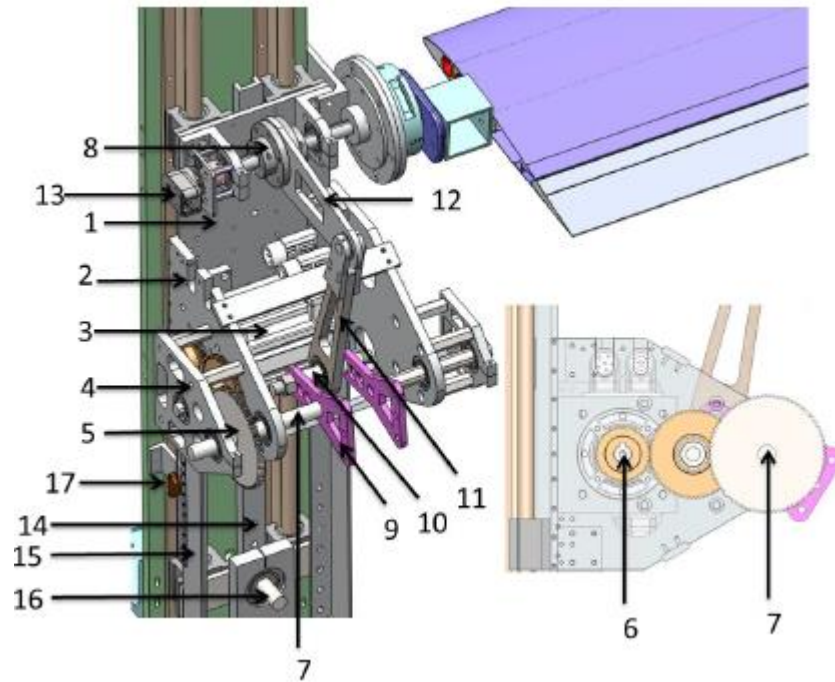


Figure 13 Port side pitch module 1. Back Plate, 2. Wall, 3. Pitch Actuator, 4. Mini Wall, 5. Gearbox, 6. Motor Shaft, 7. Drive Shaft, 8. Wing Shaft, 9. Crank, 10. Drive Pin, 11. Connecting Rod, 12. Wing Bar, 13. Spine, 14. Extension Channel, 15. Plunge Encoder [2]

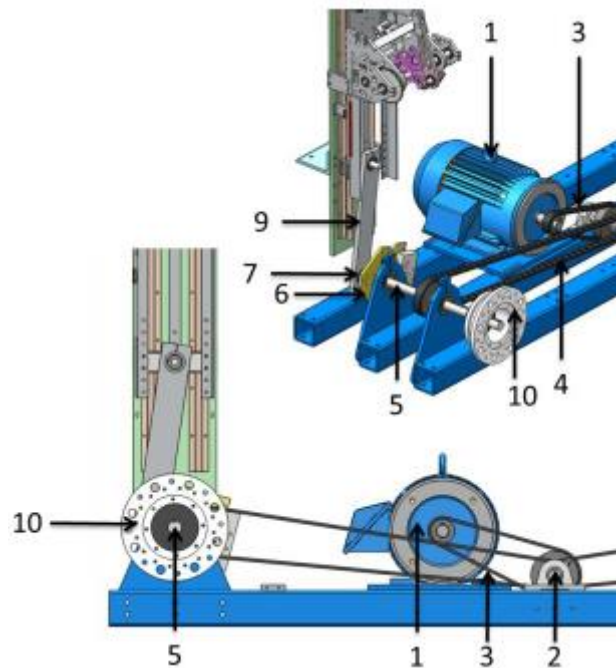


Figure 14 Plunge mechanism 1. Plunge Motor, 2. Main Drive Shaft, 3. Primary Belt Drive, 4. Secondary Belt Drive, 5. Plunge Drive Shaft, 6. Plunge Crank Wheel, 7. Plunge Crank Pin, 9. Plunge Connecting Rod, 10. Flywheel [2]

2.5 Conclusion

The different mounting systems discussed above were intended for two-degree-of-freedom motions, plunging and pitching, of airfoil. Farmer's mount system does not involve ball bearings which impart nonlinearity to the system and depending on how fast they are rotating, which depends on the load, their damping contribution differs. ^[7] The multiparameter Mount system ^[6] and the one used for testing structural nonlinearities ^[7] are may be victims of the damping fluctuation problem related to the bearings. The four bar mechanism implemented in the mount system discussed in the last subsection is a good starting point for designing a mechanism for forced excitation whose amplitude is governed by the link next to the drive shaft as long as the bearing is linear.

3. Theory

As the main theme of this project is 2D aeroelasticity the equation of motion which links the structural model to the aerodynamic model was developed. This basically relates the motion of the airfoil with the aerodynamic force. Since the structure is considered to be flexible, the aerodynamic force creates deformation which in turn changes the aerodynamic force on the system as the deformation of the blade changes the effective angle of attack at every cross-section in different ways. This is explained in detail in the next subsection. So to investigate the deep stall characteristics this equation of motion must be integrated numerically so that it is possible to see how the airfoil characteristics affect the time response of the system and accordingly set the appropriate design values to get the required result. But to do the time simulation the aerodynamic force need to be determined either through CFD/panel code simulation or experiment in the wind tunnel. For this thesis work the plan was to make use of the panel code flow analysis tool Q³UIC developed by Néstor in DTU, but the aerodynamic code is only for pitching motion. To extend the code for plunging and edgewise motions within the given time slot was difficult and hence this part of the work is still pending. However, in this section the framework for the numerical simulation is laid down with the governing equations and some theory.

3.1 Induced velocities due to elastic deformations

As mentioned before the aerodynamics of a system changes when the structure involved, for instance blade, deforms which is effected through changes in the effective angle of attack. The deformations related to the different degree of freedom induce their own change on the angle of attack. [Table 1](#) shows the variations in perceived velocity due to deformations of the rotor blade which are all based on quasi-steady thin airfoil theory. The governing equations for the Aeroelastic system were derived in the next subsection Based on the information in this table.

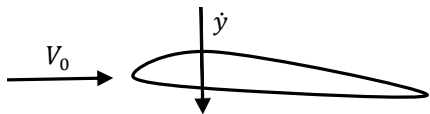

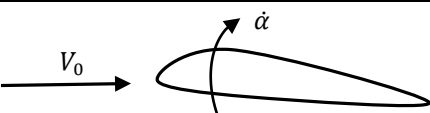
DOF	Airfoil motion	Perceived wind speed	Equivalent angle of attack
Plunging (flapwise)		$v = -\dot{y}$	$\alpha_{eq} = \frac{\dot{y}}{V_0}$
Lead-lag		$u = -\dot{x}$	$\alpha_{eq} = \frac{v}{V_0 + \dot{x}}$
Pitching		$v = \dot{\alpha}(x - ac/2)$	$\alpha_{eq} = \frac{\dot{\alpha}(x - ac/2)}{V_0}$

Table 1 Induced velocities due to deformations

3.2 Governing Equations of motion

In this subsection the governing aero-elastic equations are derived. The quasi-steady aerodynamic loads can be determined as below based on [Figure 15](#). The flap wise force F_y is always opposite to the corresponding motion in the same direction and hence acts as aerodynamic damping force.

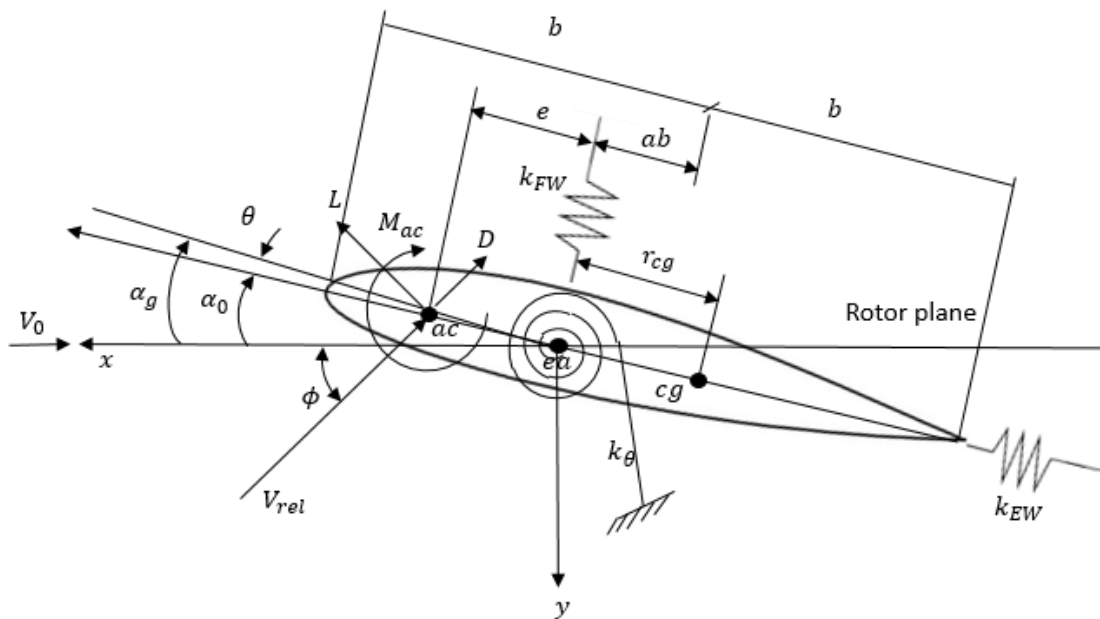


Figure 15 A 3 – DOF system

$$\tan\phi = \frac{\dot{y}}{V_0 + \dot{x}} \quad (3.1)$$

$$\alpha_g = \alpha_0 + \theta \quad (3.2)$$

$$\alpha = \phi + \alpha_g + \left(\frac{1}{2} - a\right) b \frac{\dot{\theta}}{V_0}$$

$$V_{rel}^2 = \dot{y}^2 + (V_0 + \dot{x})^2 \quad (3.3)$$

$$L(t) = 1/2 \rho V_{rel}^2 A C_l(\alpha) \quad (3.4)$$

$$D(t) = 1/2 \rho V_{rel}^2 A C_d(\alpha)$$

$$F_x = L \sin \phi - D \cos \phi \quad (3.5)$$

$$F_y = -(L \cos \phi + D \sin \phi)$$

$$M_{ea} = -M_{ac} + F_y e \times \cos \alpha_g = F_y e \times \cos \alpha_g, \text{ for symmetric or uncambered airfoil} \quad (3.6)$$

Here A = Airfoil area = $c \times l$, c = Chord length, l = Span of airfoil = $1m$, e = Eccentricity of aerodynamic center from elastic axis, and $M_{ac} = \frac{1}{2} \rho V_{rel}^2 A C_{M_{ac}}$ = Aerodynamic moment independent of α (*NB: $C_{M_{ac}} = 0$ for symmetric or uncambered airfoil*).

Having known the expressions for the aerodynamic loads, Lagrange's Equations were used to describe system dynamics. Figure 16 shows the three degrees of freedom used to describe the system. The generalized coordinates were defined as, $q_1 = x$, $q_2 = y$, and $q_3 = \alpha_g$ and generalized forces as $Q_1 = F_x$, $Q_2 = F_y$, $Q_3 = M_{ea}$.

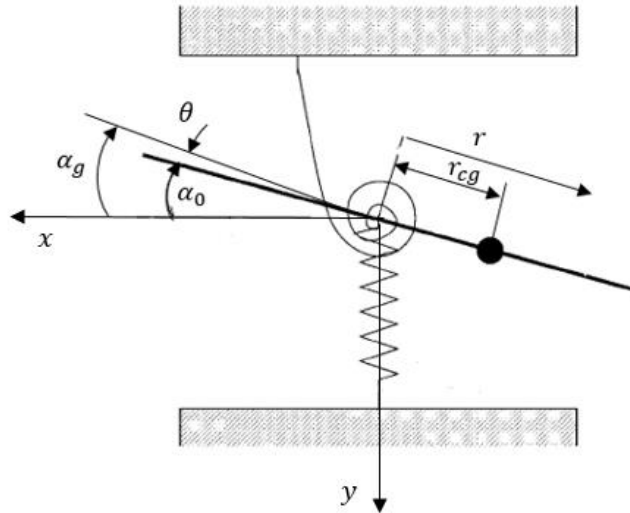


Figure 16 System DOF

The displacement of any point on the chord can be expressed as

$$\mathbf{p} = u\mathbf{i} + v\mathbf{j}$$

\mathbf{i} and \mathbf{j} are unit vectors in the horizontal and vertical directions respectively. u & v can be inferred from geometry (See Figure 15),

$$\left. \begin{aligned} u &= r - r \cos \alpha_g + x \approx x \\ v &= r \sin \alpha_g + y \approx r \alpha_g + y \end{aligned} \right\} \text{ for } \alpha_g = \theta + \alpha_0 \ll 1$$

The kinetic and potential energy can be written in terms of the generalized coordinates as under with ρ as the mass per unit chord length.

$$\begin{aligned}
T &= \frac{1}{2} \int_{chord} \left[\left(\frac{du}{dt} \right)^2 + \left(\frac{dv}{dt} \right)^2 \right] \rho dx \\
&= \frac{1}{2} \int_{chord} \left[\dot{x}^2 + (\dot{y} + r\dot{\theta})^2 \right] \rho dx \\
&= \frac{1}{2} \int_{chord} \left[\dot{x}^2 + \dot{y}^2 + 2r\dot{y}\dot{\theta} + r^2\dot{\theta}^2 \right] \rho dx \\
&= \frac{1}{2} \dot{x}^2 \int_{chord} \rho dx + \frac{1}{2} \dot{y}^2 \int_{chord} \rho dx + \frac{1}{2} 2\dot{y}\dot{\theta} \int_{chord} r \rho dx + \frac{1}{2} \dot{\theta}^2 \int_{chord} r^2 \rho dx \\
&= \frac{1}{2} \dot{x}^2 m + \frac{1}{2} \dot{y}^2 m + \frac{1}{2} 2\dot{y}\dot{\theta} (-mr_{cg}) + \frac{1}{2} \dot{\theta}^2 I_{ea} \\
\boxed{T} &= \boxed{\frac{1}{2} m \dot{x}^2 + \frac{1}{2} m \dot{y}^2 - \dot{y}\dot{\theta} m r_{cg} + \frac{1}{2} I_{ea} \dot{\theta}^2}
\end{aligned}$$

Potential energy

$$\boxed{U = \frac{1}{2} k_x x^2 + \frac{1}{2} k_y y^2 + \frac{1}{2} k_\theta \theta^2}$$

And dissipative energy

$$\boxed{D = \frac{1}{2} c_x \dot{x}^2 + \frac{1}{2} c_y \dot{y}^2 + \frac{1}{2} c_\theta \dot{\theta}^2}$$

Applying Lagrange's equation for each DOF,

$$\begin{aligned}
-\frac{d}{dt} \left(\frac{\partial(T-U)}{\partial \dot{x}} \right) + \frac{\partial(T-U)}{\partial x} - \frac{\partial D}{\partial \dot{x}} + F_x &= 0 \quad \Rightarrow \quad -\frac{d}{dt} (m\dot{x}) - k_x x - c_x \dot{x} + F_x = 0 \\
-\frac{d}{dt} \left(\frac{\partial(T-U)}{\partial \dot{y}} \right) + \frac{\partial(T-U)}{\partial y} - \frac{\partial D}{\partial \dot{y}} + F_y &= 0 \quad \Rightarrow \quad -\frac{d}{dt} (m\dot{y} - mr_{cg} \dot{\theta}) - k_y y - c_y \dot{y} + F_y = 0 \\
-\frac{d}{dt} \left(\frac{\partial(T-U)}{\partial \dot{\theta}} \right) + \frac{\partial(T-U)}{\partial \theta} - \frac{\partial D}{\partial \dot{\theta}} + M_{ea} &= 0 \quad \Rightarrow \quad -\frac{d}{dt} (mr_{cg} \dot{y} + I_{ea} \dot{\theta}) - k_\theta \theta - c_\theta \dot{\theta} + M_{ea} = 0
\end{aligned}$$

In matrix form

$$\underbrace{\begin{bmatrix} m & 0 & 0 \\ 0 & m & -mr_{cg} \\ 0 & -mr_{cg} & I_{ea} \end{bmatrix}}_M \underbrace{\begin{bmatrix} \ddot{x} \\ \ddot{y} \\ \ddot{\theta} \end{bmatrix}}_{\dot{q}} + \underbrace{\begin{bmatrix} c_x & 0 & 0 \\ 0 & c_y & 0 \\ 0 & 0 & c_\theta \end{bmatrix}}_C \underbrace{\begin{bmatrix} \dot{x} \\ \dot{y} \\ \dot{\theta} \end{bmatrix}}_{\dot{q}} + \underbrace{\begin{bmatrix} k_x & 0 & 0 \\ 0 & k_y & 0 \\ 0 & 0 & k_\theta \end{bmatrix}}_K \underbrace{\begin{bmatrix} x \\ y \\ \theta \end{bmatrix}}_q = \underbrace{\begin{bmatrix} F_x \\ F_y \\ M_{ea} \end{bmatrix}}_F \quad (3.7)$$

Or in compact form equation (3.7) can be rewritten as

$$M\ddot{q} + C\dot{q} + Kq = F(t) \quad (3.8)$$

The damping term C is referring to structural damping, M mass, K stiffness, and F is aerodynamic loads. This equation has been used for the numerical simulation in this thesis along with its other version (see section 5.2) that includes a modification in which the aerodynamic forces are redistributed to take into account the changes in direction of vibration with respect to the rotor plane. In reality this change in direction of vibration is spontaneous, but in wind tunnel experiment

the airfoil model is supposed to be forced to vibrate in a certain direction relative to the rotor plane by the use of the mount system developed in this thesis work as described in the next section, it is not tried yet though owing to time constraint.

4. Experimental Set-up

The Red Wind Tunnel facility at DTU (See [Figure 17](#)) is to be redesigned in order to increase its capability for carrying out tests for deep stall flow by increasing its test section of $0.5 \times 0.5 \text{ m}^2$ and implementing a new mount system which was developed during the course of this thesis work. The new mount system described here adds degree of freedom to the airfoil model in addition to allowing forced vibration. An effort has been put to keep its weight as minimum as possible. As it is now, part of the system which is involved in the dynamics weighs 1166.31 grams (See [Appendix 8.4](#), for detail list of mass of parts).



Figure 17 The Red Wind Tunnel facility at DTU

4.1 Mount system Overview

The 3 degree of freedom (DOF) mount system developed here is a device for conducting aeroelasticity experiments under steady or unsteady aerodynamics in the red wind tunnel facility at DTU which is to be redesigned. It allows pitching, plunging and edgewise motions either simultaneously or independently. Besides, given the fact that the stall induced vibrations are dependent on the direction of vibration relative to the rotor plane, ^[15] the device is equipped with the capability that it is possible to force direction of vibration in a particular direction as well by rotating the plunging and edgewise springs (see [Section 4.4](#)). More importantly, the device was designed with the capability to vary the stiffness of each DOF and the airfoil model itself without much effort and quickly so as to facilitate conducting parametric study during the experiment. There is a servo motor, not shown in the illustrations here, which is connected to the worm through a flexible wire so as to change the geometrical angle of attack, but kept away from the entire

mount system. There are three major subassemblies that add up to the 3-DOF mount system shown in Figure 18, namely the frame, pitch module, and plunging & lead-lag module. They are explained in detail in the upcoming subsections. In terms of the device's position in the wind tunnel, the entire components are supposed to be outside the test section, except the airfoil model including the two laser sensors as well which can be mounted on rigid walls of the wind tunnel. More pictures of the device can be seen in the Appendix.

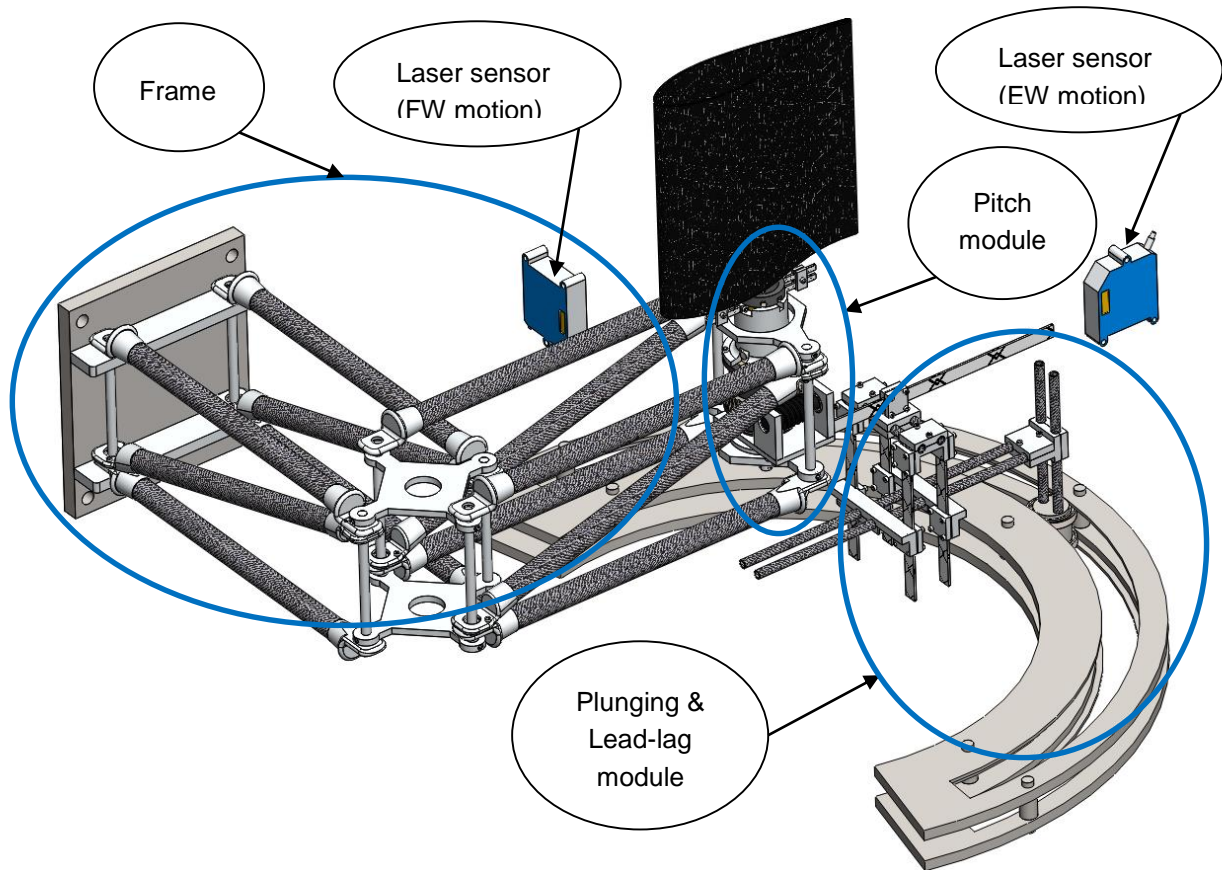


Figure 18 3D model of the mount system and its major subassemblies

4.2 Frame

The frame as shown in Figure 19 comprises rigid carbon fiber rods (2) & (3), a steel base plate (1) to attach the mount system to a rigid wall, six aluminum plates (3), eight aluminum shafts (4), and ball bearings. As opposed to what has been mentioned in section 2.1 related to the introduction of a variable damping, proportional to the aerodynamic load, that comes along with using bearings, ^[1] their implementation here has barely any damping effect to the device. Because the angular motions at each pivot joints are only in the linear approximation range. It has three pivot joints which give rise to two translational motions at the pitch module corresponding to the plunging (FlapWise – FW) and lead-lag (EdgeWise – EW) motions. Besides, it also provides support for the pitch module which holds the airfoil model (See section 4.3).

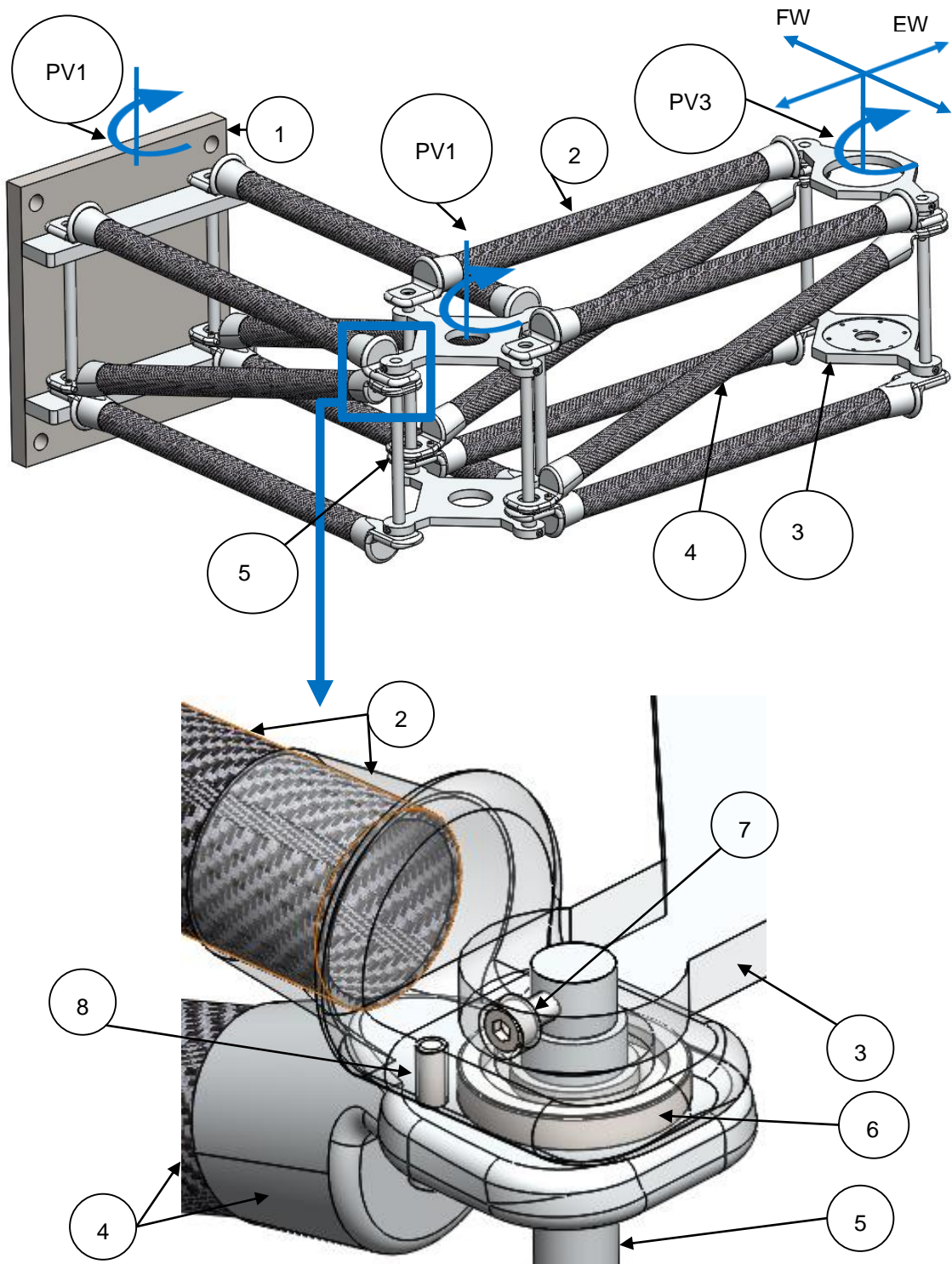


Figure 19 Frame for the mount system and one of its Pivot joints detail view. 2. Carbon fibre rod and its aluminium fixture, 3. Aluminium plate, 4. Carbon fibre stiffener and its aluminium fixture, 5. Shaft, 6. SKF ball bearing, 7 & 8. Hexagonal socket head screws.

4.3 Pitch module

The pitch module is shown in [Figure 20](#) and [Figure 21](#) with its parts explained below and alongside the pictures. This entire module is mounted on the bottom aluminum plate of the frame at the 3rd pivot joint. (Cf. [Figure 19](#))

9. Model fixture – this is where the airfoil model is attached. It is made of polyoxymethylene (POM).
10. Torsion spring – is a beam of cross section $2 \times 5 \text{ mm}^2$ made of either steel or carbon fiber. It is acting like a cantilever beam so that the bending constant (EI) is the stiffness of the spring. Its length can be adjusted, thereby vary its stiffness, by moving the spring fixtures (14). (See [Figure 22](#))
11. Pin locking shaft and model fixture – as shown in [Figure 18](#) the airfoil model gets its torsional degree of freedom (DOF) through the rotating shaft (12) mounted on two SKF bearings (13). Hence the pin transmits motion between shaft and model fixture (9) by locking them together.
12. Shaft – mounted as a simply supported beam so as to ensure upright position of airfoil model and extended as a cantilever beam. It provides torsional DOF.
13. SKF Bearings – for torsional DOF
14. Torsion spring fixtures – aluminum plates to set the torsional stiffness.
15. Slot – it is used to lock the torsional DOF along with a corresponding recess on the model fixture (9) with a rectangular shaft (not shown on the figures).
16. Encoder fixture – made from aluminum. It accommodates the encoder.
17. Encoder – SCH24 encoder
18. Teflon bearing – provides the pitching DOF while setting the geometrical angle of attack of airfoil model.
19. Steel interface – the entire load is transmitted to the sensor, which is to be put inside the sensor fixture (19), through a small contact area at the interface between the two (See [Figure 22](#)). It is made of steel to make sure that part of the load is not lost in the way due to deformation.
20. Sensor fixture – this is where the sensor is kept. It is made of aluminum (AL7075).
21. Worm wheel fixture – supports wheel of the worm gear. It is made from POM.
22. Worm gear – the pitch angle of the airfoil model is set through this gear. Its self-locking property enables to keep the airfoil at any specific pitch angle. Both the wheel and worm are made from POM.
23. Teflon bearing – the Worm wheel fixture (21) is simply supported on two such Teflon bearings (together with the other Teflon bearing (18)). They were chosen to take advantage of their light weight.
24. Worm shaft support – aluminum plates to support the simply supported worm shaft through SKF bearings on either end of the worm. They are rigid relative to the worm (see the explanation for (25)).
25. Pitch module support plate – parts from (9) to (23), except the steel interface (19) and sensor fixture (20), are involved in the pitching motion, but they all move relative to this support and worm shaft support (24), which is also supported by this aluminum plate. The latter two got their rigidity with respect to those involved in the pitching motion through the sensor fixture (20) which is also the only part to connect them to the rest of the mount system.
26. Sensor fixture support – it is made of aluminum. Parts from (9) to (25) contact with the rest of the mount system only through this support which is bolted to the sensor fixture (20).

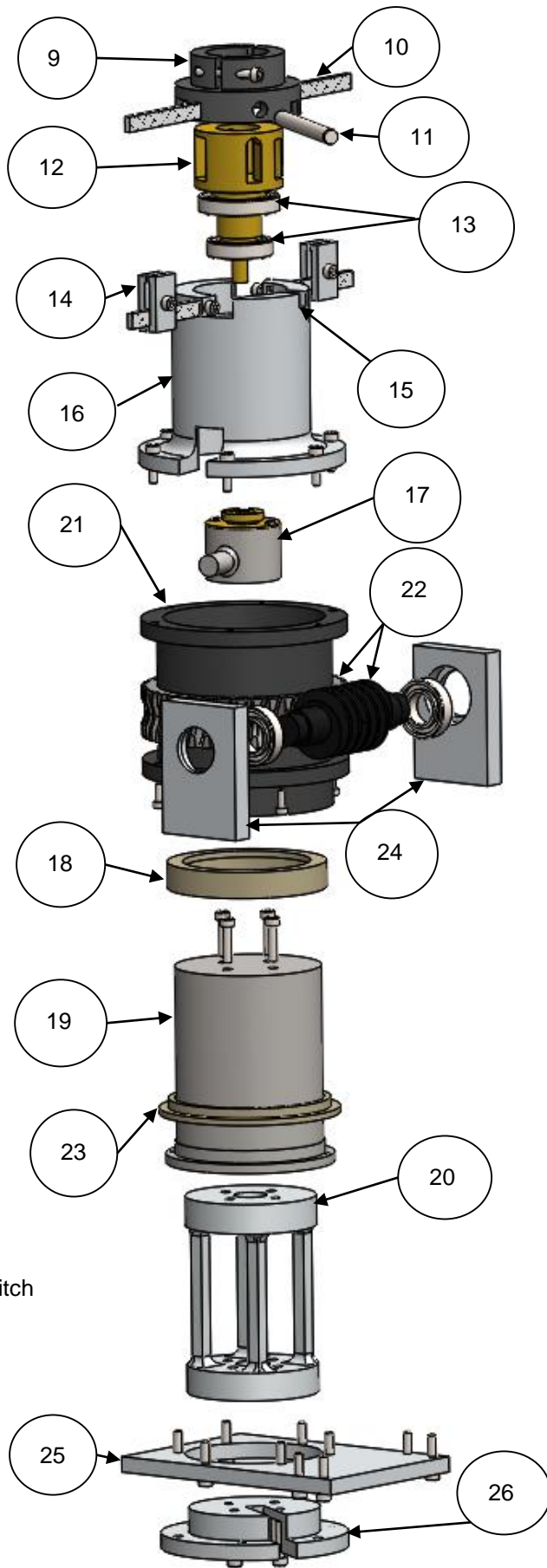


Figure 20 Exploded view of Pitch module

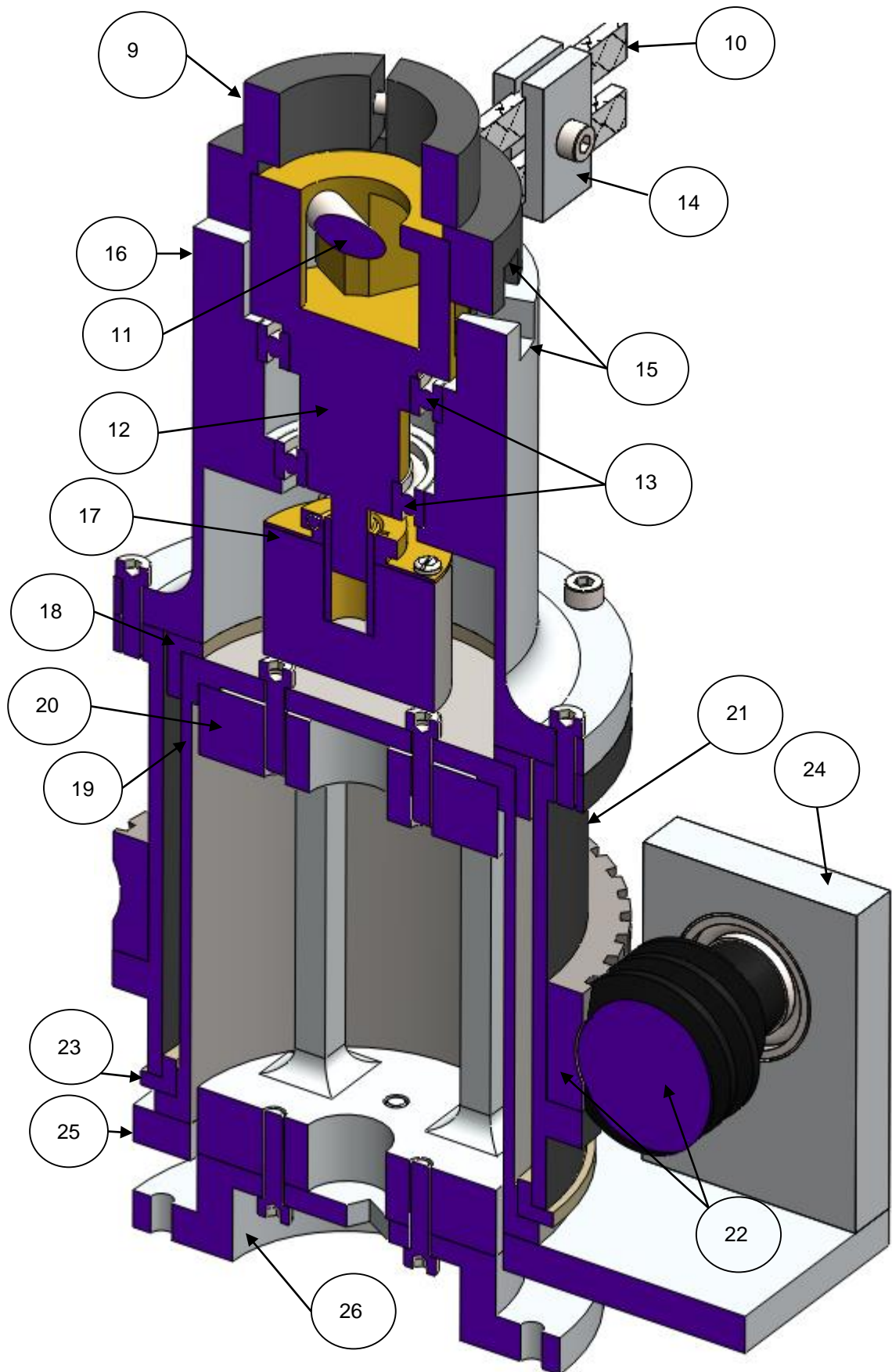


Figure 21 Sectional view of pitch module of the mount system

4.3.1 Torsional stiffness

The torsional stiffness is represented by four beams made from carbon fiber with their lengths to be adjustable as shown in Figure 22. Each beam is deflected as a cantilever beam with the deflection slope being zero at both ends and hence they can be approximated by four linear springs in parallel with identical stiffness given by equation (4.1). The fact that there are two such springs on either end is meant to soften the springs as the deflection of each beam is compensated by virtually equal and opposite deflection of the other beam in the pair (See Figure 22 C). This is equivalent to reducing the stiffness of each beam by half so that their equivalent stiffness is the arithmetic sum of all four which is equal to k_t .

$$k_t = 2 \times \frac{12EI}{x^3} = \frac{24EI}{x^3} \quad (4.1)$$

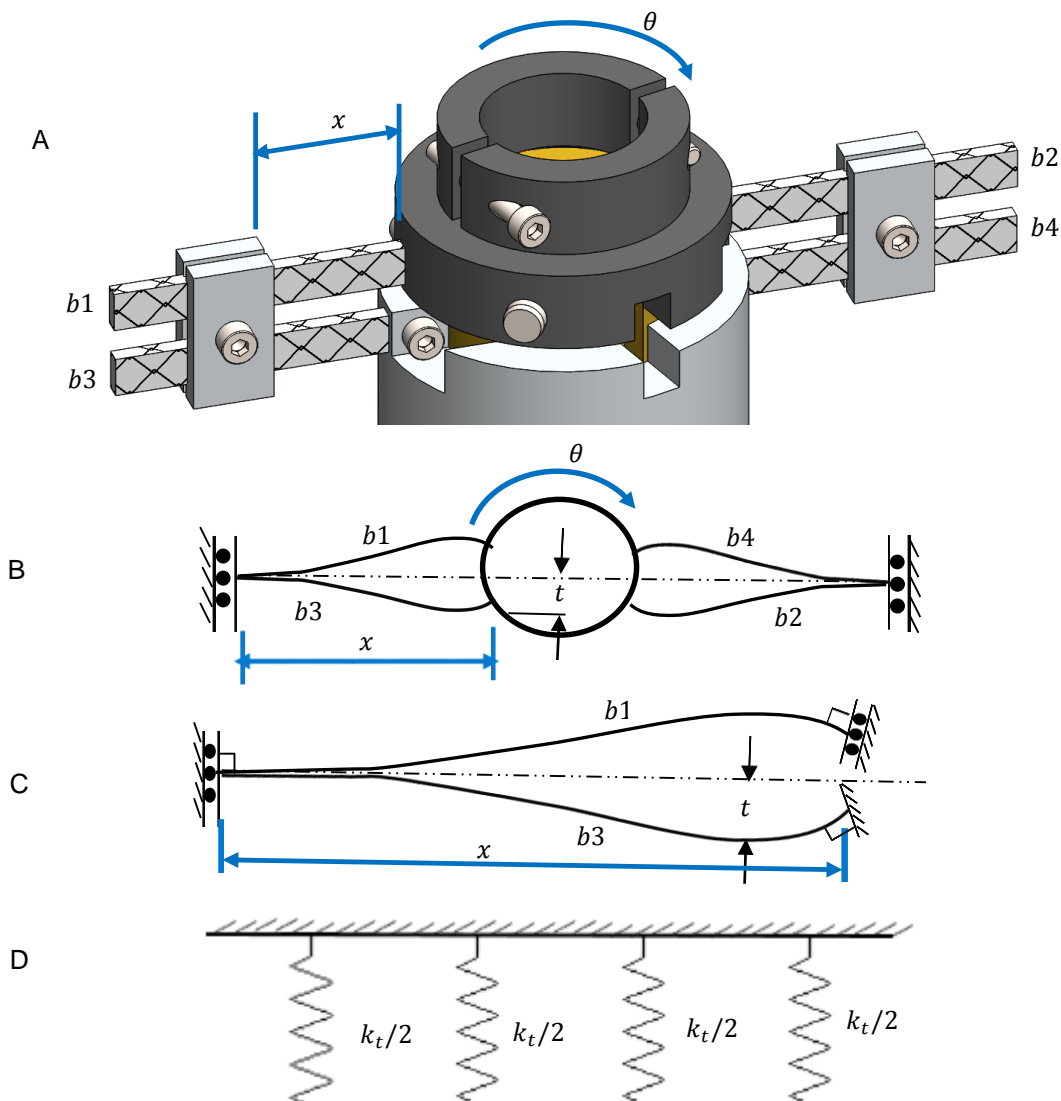


Figure 22 A – Torsional stiffness before deformation (trimetric view), B – schematic representation of torsional stiffness after deformation (top view), C – Exaggerated view of deflection on one side, D – linear approximation of angular deflection

4.4 Plunging and lead-lag module

This module consists of the flapwise and edgewise springs in a way their stiffness can be varied at will by changing the length of the corresponding spring plate which are made of either steel or carbon fiber. In [Figure 23](#) part 33 corresponds to the flapwise spring plate while part 34 is for edgewise spring. To vary the flapwise stiffness part 38 can be slid back and forth on the rigid carbon rods (part 35). Likewise, the edgewise stiffness can be varied by moving this same part vertically up and down. In fact when there is a need for experimenting with only one or two DOF, part 38 can be moved to its extreme ends so as to lock the other DOF which is not going to involve in the study. To this end [Figure 24](#) shows the case when both the flapwise and edgewise springs are stiffened to rigidity so that only pitching motion is allowed.

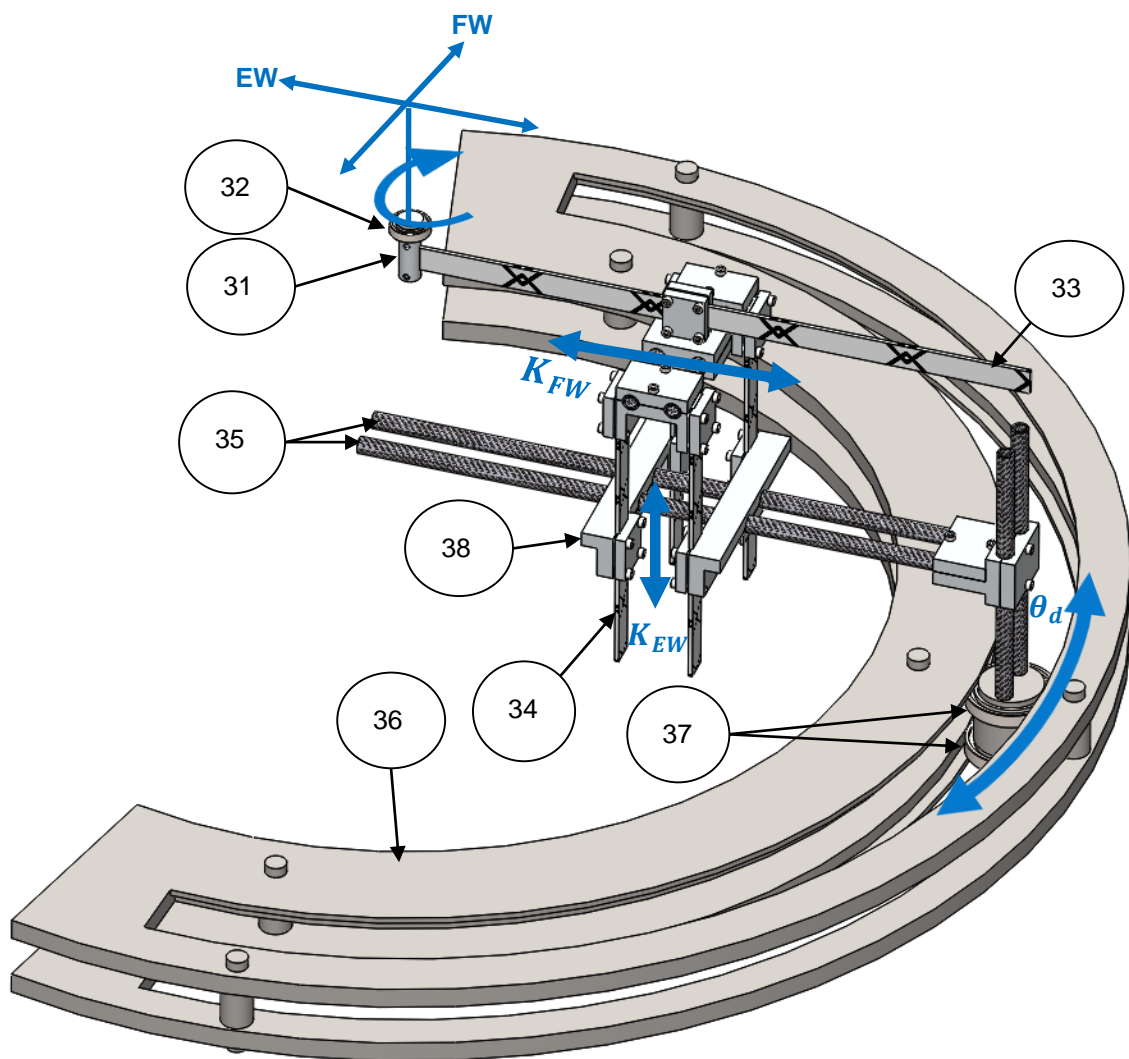


Figure 23 Plunging and lead-lag Spring subassembly: 31. Flapwise (FW) spring (33) fixture, 32. SKF bearing, 33. Flapwise spring, 34. Edgewise spring, 35. Rigid carbon rods, 36. Steel plates, 37. SKF bearings, 38. Edgewise (EW) spring fixture.

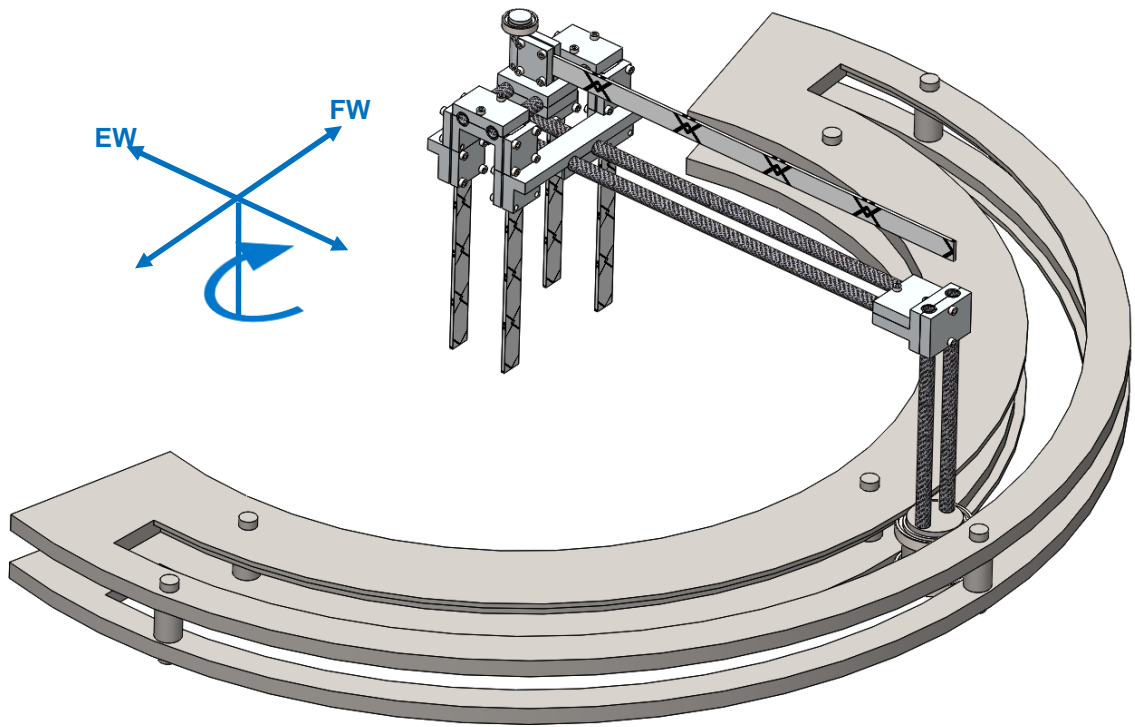


Figure 24 Plunging and lead-lag Spring subassembly – locking the plunging and lead-lag motions.

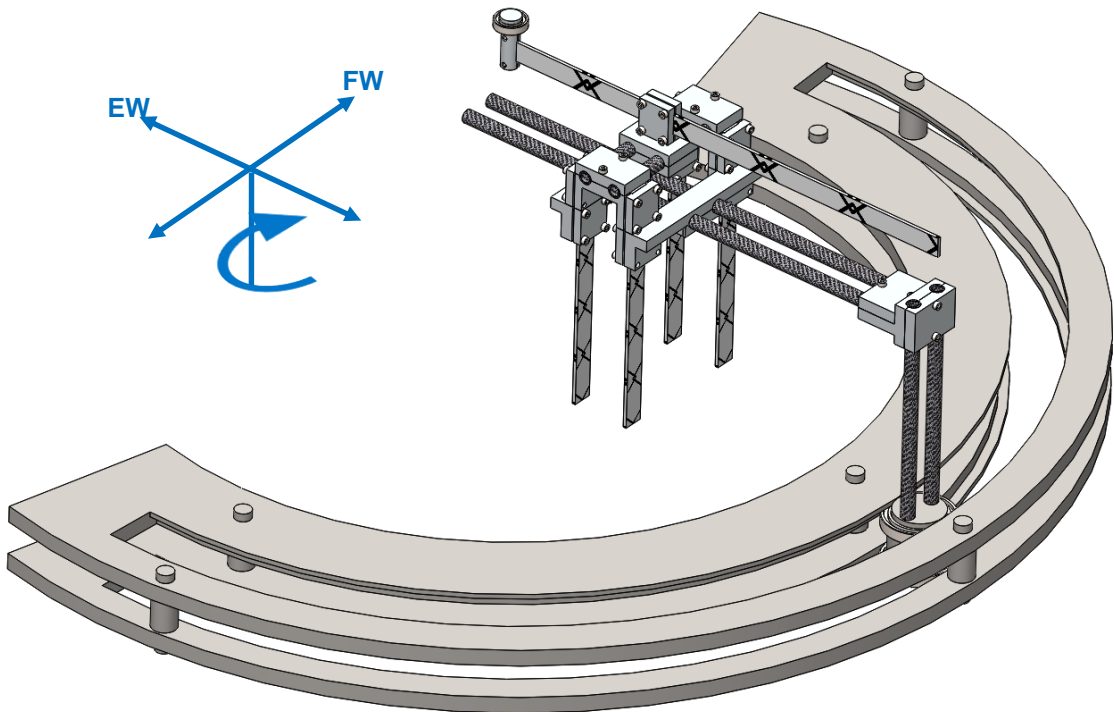


Figure 25 Plunging and lead-lag Spring subassembly with only one DOF (Plunging)

In another case [Figure 25](#) and [Figure 26](#) show that only the edgewise or flapwise motion respectively is locked. On the other hand, there is also a provision for rotating the springs (see the bearings – part 37) so that the direction of vibration can be forced to be different from that of the usual flapwise and edgewise oscillations. For instance, [Figure 27](#) shows one instance of its implementation in the wind tunnel in which the effective direction of oscillation is now at 45° and 135° relative to the rotor plane corresponding to the edgewise and flapwise motion respectively. The latter enables to explore the behavior of aerodynamic damping in relation to direction of vibration with respect to rotor plane, see section 5.2 for a detail discussion. The stiffness of the spring is determined in the same manner as explained for the torsional spring in the previous subsection. Here the edgewise spring is represented by four beams and the flapwise by just one beam.

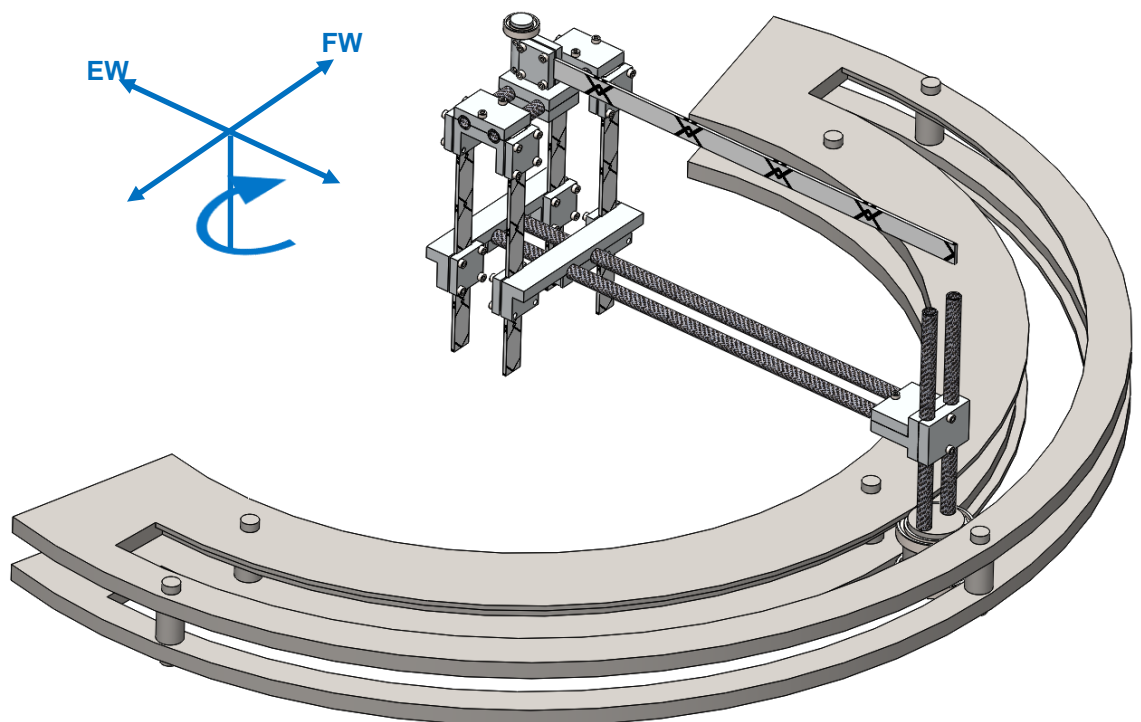


Figure 26 Plunging and lead-lag Spring subassembly with only one DOF (Lead-lag)

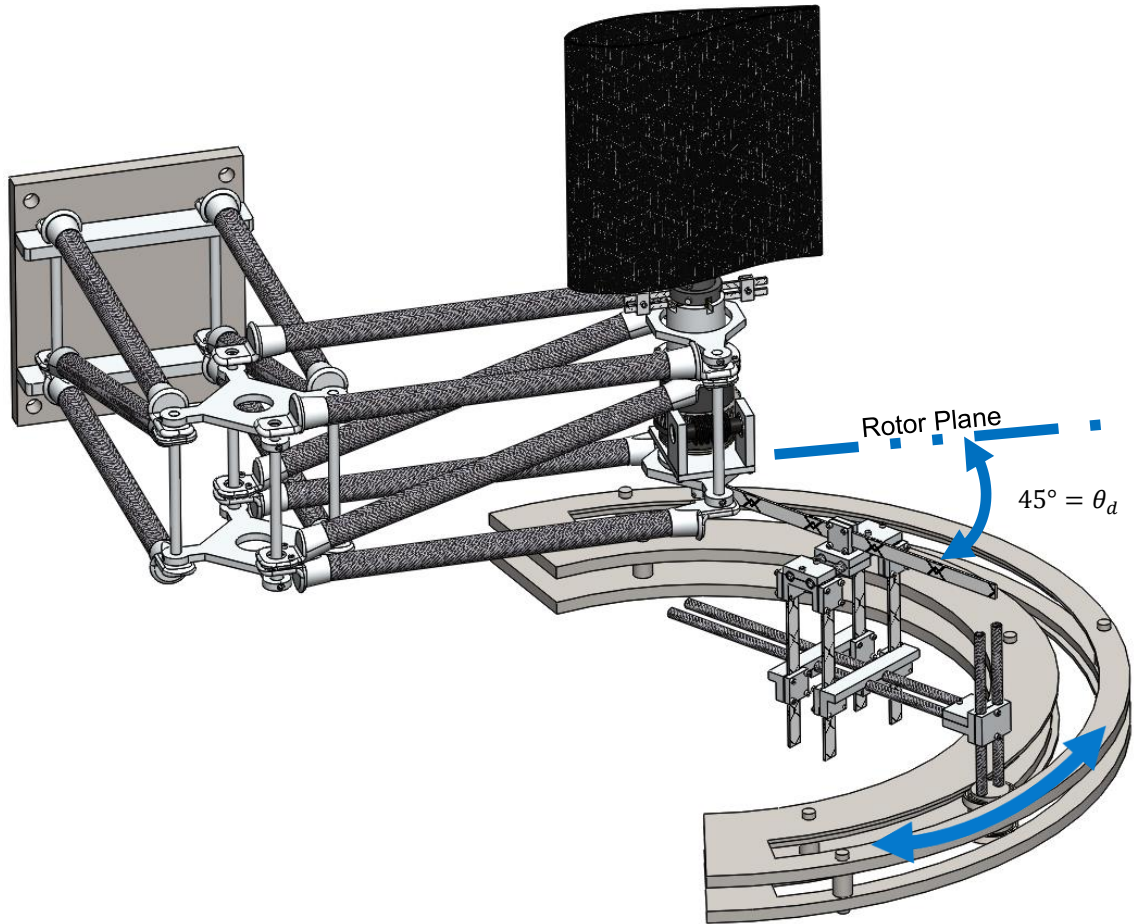


Figure 27 Plunging and lead-lag Spring subassembly rotated to force vibration in a certain direction with respect to rotor plane

5. Analytical Results, Outcome and Relevance

In this section a case was taken to reflect on the main ideas like how the use of dynamic stall model makes a difference on simulation results of system response and more importantly the effect of direction of vibration relative to rotor plane on the aerodynamic damping based on the paper *Aeroelastic instability problems for wind turbines* by M. H. Hansen in 2007. ^[15] [Table 2](#) summarizes the data used for the simulation of the case in addition to the airfoil data from `tjaere11_ds.dat` (Taken from 2MW Tjaereborg wind turbine blade). The given steady state airfoil data enables to determine the aerodynamic loads so as to try the time simulation scheme developed based on the equation of motion derived following Lagrangian mechanics in section 3.2. It comprises lift coefficients for different flow conditions as shown in [Figure 28](#). The corresponding columns are indicated within the bracket. The plot also shows the curve that indicates the degree of separation at each angle of attack.

Parameters	Figures	Centers
Airfoil mass	1 kg	Aerodynamic center at c/4 from LE
Airfoil chord length	0.2 m	
Airfoil span	1 m	Elastic axis at c/2
Spring stiffness	k_{FW} , k_{EW} [N/m] and k_{θ} [N/m]	Center of gravity at c/4 from TE
Wind speed	2 m/s	
Initial displacement (q_0)	[0.02 m, 0.02m, 0.02rad]	
Assumption	$C_d = 0$ & $\alpha_g = [0^\circ \ 15^\circ]$	

Table 2 System parameters

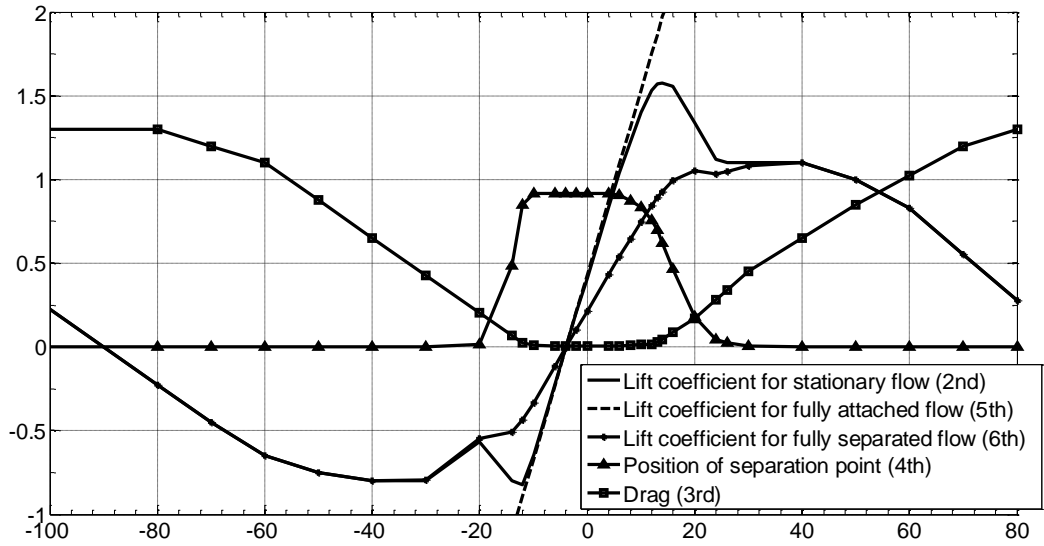


Figure 28 Lift curves

5.1 Dynamic stall model (DSM)

For wind turbines the instantaneous change in angle of attack due to wind variation is not reflected on the loads right away, rather the loads change after a time delay proportional to the chord divided by the relative velocity seen at the point in question ^[19]. This time delay effect can be modelled differently depending on whether the boundary layer flow is attached (Theodorsen theory) or partly separated (the Øye model ^[18]). For instance, the latter is believed to represent the real scenario in wind turbines, wherein separation starts at the trailing edge and gradually increases upstream when the angle of attack increases, ^[19] and hence Øye dynamic stall model was implemented here to generate the dynamic airfoil data from the steady state airfoil data. This model ensures an overall positive slope of the lift curve in the stall region (See Figure 29) and hence a positive aerodynamic damping as per the discussion later in this section (See equation (5.12)). As shown in Figure 28 the static airfoil data has negative slope in this region. In this model the degree of separation f_s is defined as in equation (5.2) to approximate the lift coefficient from those of a fully separated flow ($C_{l,fs}(\alpha)$) and fully attached flow ($C_{l,inv}(\alpha)$).

$$C_l = f_s C_{l,inv}(\alpha) + (1 - f_s) C_{l,fs}(\alpha) \quad (5.1)$$

Where f_s is given by,

$$\frac{df_s}{dt} = \frac{f_s^{st} - f_s}{\tau} \quad (5.2)$$

Or analytically as

$$f_s(t + \Delta t) = f_s^{st} + (f_s(t) - f_s^{st})\exp(-\Delta t/\tau) \quad (5.3)$$

Here $\tau = 4c/V_{rel}$ is time constant describing how fast f_s gets back to the static value f_s^{st} after each time step. In the time simulation (ode45 of MATLAB) the initial value, $f_s(0)$ was taken as f_s^{st} .

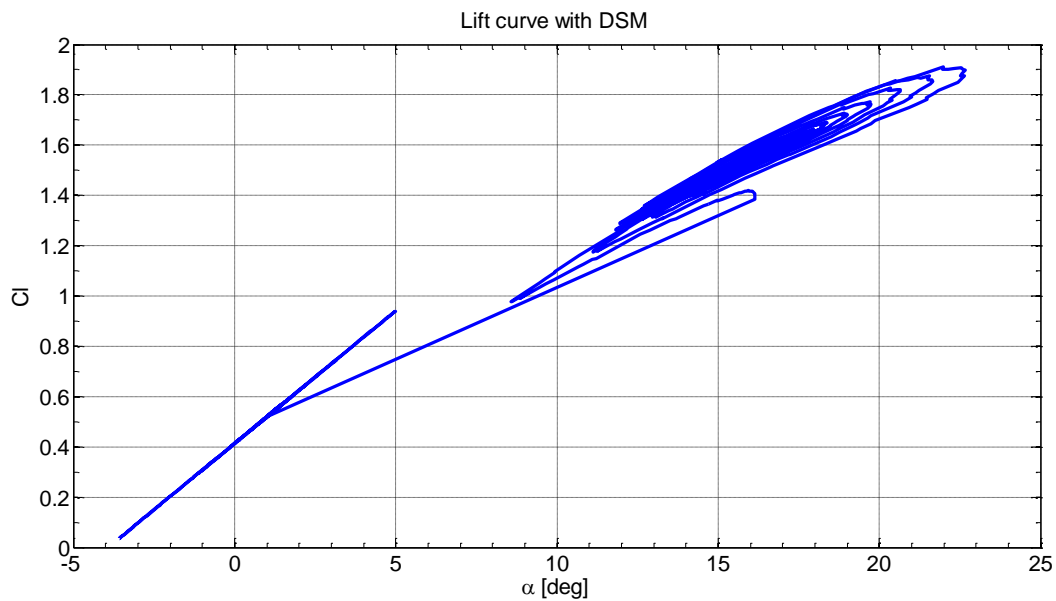


Figure 29 Simulated Lift curve of DSM

5.1.1 Response of system for $\alpha_g = 0^\circ$

Figure 30 shows the time response corresponding to the 3 DOF motion of the airfoil at $\alpha_g = 0^\circ$. As expected there is no difference in the output motion with or without DSM as the angle of attack is very low. Which means the DSM does not have any effect as the angle of attack is below stall. The lead-lag response in Figure 30 shows the low damping in the lead-lag motion, as opposed to the plunging and pitching motions, which is also evident in Figure 33 in which the damping is close to zero at $\theta_d = 0$.

5.1.2 Response of system for $\alpha_g = 15^\circ$

Here the effect of DSM is apparent as shown in Figure 31 as the angle of attack goes past stall. The responses from steady state airfoil data do not seem natural, but the DSM gives realistic response as reflected in the same plots in which the vibration is damped out because of the overall positive slope of the lift curve that give rise to a positive aerodynamic damping. Besides, as expected the fact that the lead-lag motion is less damped than the plunging motion is clearly shown on the plots.

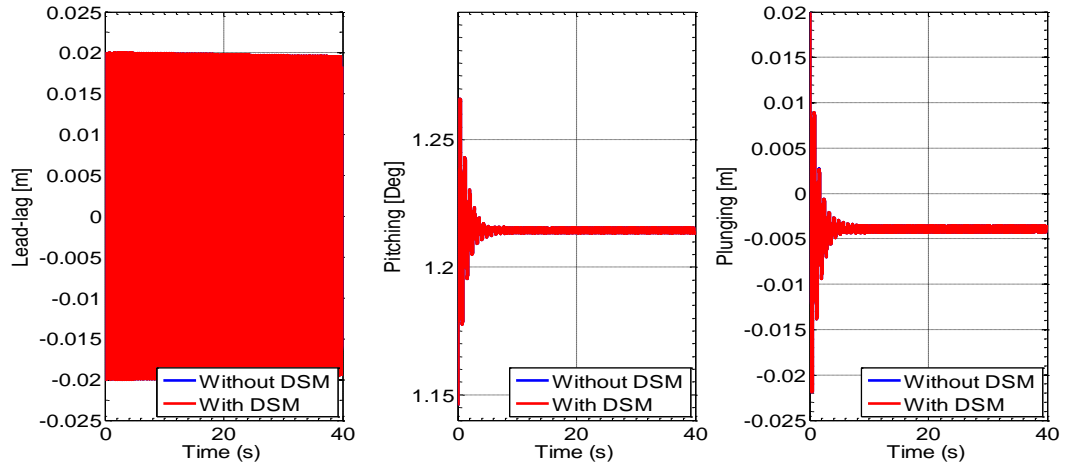


Figure 30 System response for zero geometrical angle of attack

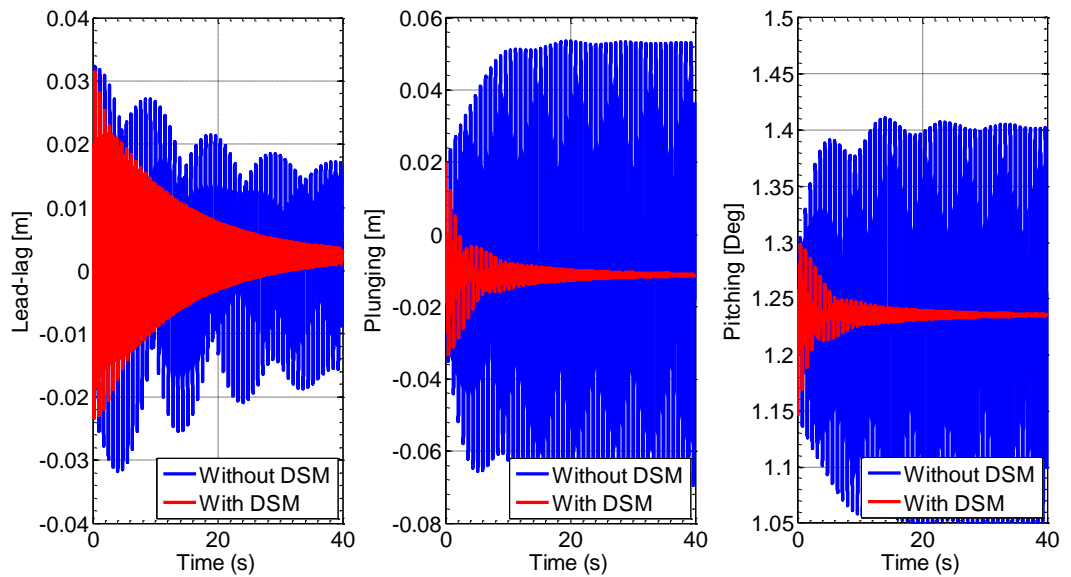


Figure 31 System response for 15° geometrical angle of attack

5.2 Direction of vibration

The direction of vibration in the context of this thesis is referring to the angle θ_d in Figure 32 relative to the rotor plane. Physically it means that the blade is now oscillating in a direction neither parallel nor perpendicular to the rotor plane. On the real turbine it is the pre-twist that causes the rotation of the principal bending axes at every radial section of the blades. [15, 25] Besides, the edgewise and flapwise rotor whirling modes can also influence the direction of blade vibration. [26, 27] The quasi-steady aerodynamic forces that are parallel and perpendicular to θ_d were obtained from lift and drag as under. The aero-elastic modelling was based on the textbook in the reference [19].

$$\tan\phi = \frac{\dot{x}\sin\theta_d + \dot{y}\cos\theta_d}{V_0 + \dot{x}\cos\theta_d - \dot{y}\sin\theta_d} \quad (5.4)$$

$$\alpha_g = \alpha_0 + \theta$$

$$\alpha = \phi + \alpha_g + \left(\frac{1}{2} - a\right) b \frac{\dot{\theta}}{V_0} \quad (5.5)$$

$$V_{rel}^2 = (\dot{x}\sin\theta_d + \dot{y}\cos\theta_d)^2 + (V_0 + \dot{x}\cos\theta_d - \dot{y}\sin\theta_d)^2 \quad (5.6)$$

$$L(t) = 1/2\rho V_{rel}^2 AC_l(\alpha) \quad (5.7)$$

$$D(t) = 1/2\rho V_{rel}^2 AC_d(\alpha)$$

$$F_x = L \sin(\phi - \theta_d) - D \cos(\phi - \theta_d) \quad (5.8)$$

$$F_y = -(L \cos(\phi - \theta_d) + D \sin(\phi - \theta_d))$$

$$M_{ea} = -M_{ac} + F_y e \times \cos(\alpha_g + \theta_d) \quad (5.9)$$

$$= F_y e \times \cos(\alpha_g + \theta_d), \text{ for symmetric or uncambered airfoil}$$

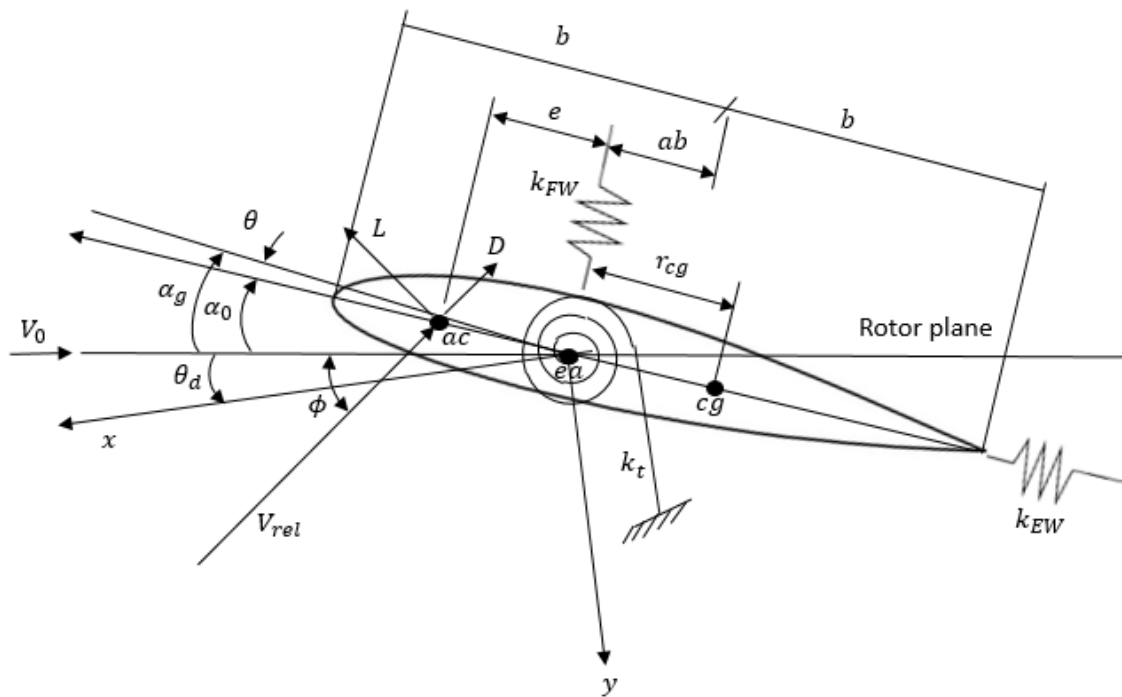


Figure 32 A 3 – DOF system

5.3 Aerodynamic damping vs. direction of vibration

Referring to Figure 32, the aerodynamic force in the direction of vibration (Cf. lead-lag motion, see Appendix 8.2) is

$$F_x = 1/2\rho V_{rel}^2 A [C_l(\alpha) \sin(\phi - \theta_d) - C_d(\alpha) \cos(\phi - \theta_d)] \quad (5.10)$$

Linearizing this force using Taylor expansion about $\dot{x} = 0$, as shown by M. H. Hansen^[15].

$$F_x = F_0 - \eta \dot{x} \quad (5.11)$$

Where the damping coefficient is

$$\eta = \frac{1}{4} \rho A V_{rel,0} [C_d(3 + \cos(2\theta_d - 2\phi_0)) + C_l'(1 - \cos(2\theta_d - 2\phi_0)) + (C_l + C_d') \sin(2\theta_d - 2\phi_0)] \quad (5.12)$$

Figure 33 shows a plot of this coefficient against the direction of vibration in which the damping is highly negative around $\theta_d = -36^\circ$ owing to domination of the third term within the square bracket in equation (5.12) and the maximum around $\theta_d = 52^\circ$. The lead-lag time response at these two particular directions of vibration were determined and shown in Figure 34 for geometrical angle of attack $\alpha_g = 0^\circ$. The response is damped out right away for the vibration in the $\theta_d = 52^\circ$ direction as opposed to the one in the $\theta_d = -36^\circ$ direction. But the situation in the case of $\alpha_g = 20^\circ$ is not so obvious (Cf. Figure 35). The ambiguity may be attributed to the fact that the damping coefficient in equation (5.12) was derived based on quasi-steady-state airfoil data, meaning the response from DSM in Figure 35 is not expected to reflect the effect of aerodynamic damping predicted by this coefficient. Besides the response from steady-state airfoil data is not realistic (See section 5.1).

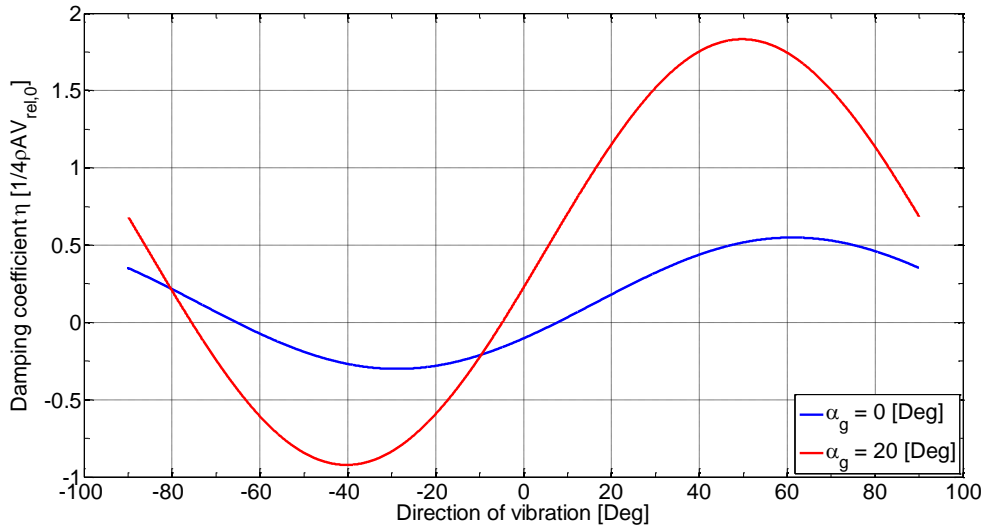


Figure 33 Aerodynamic damping

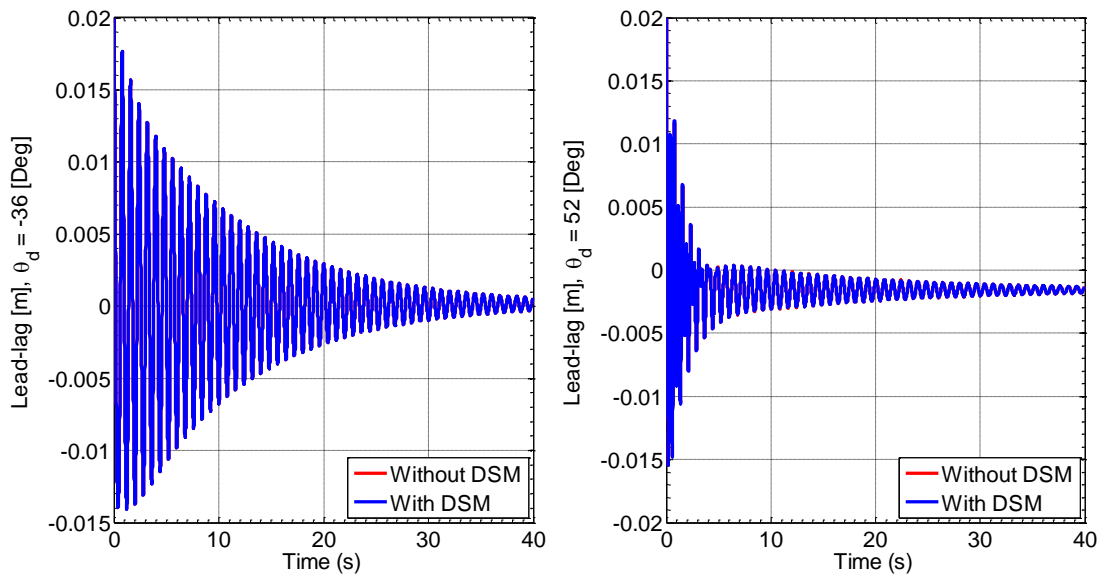


Figure 34 Lead-lag time response at zero geometrical angle of attack

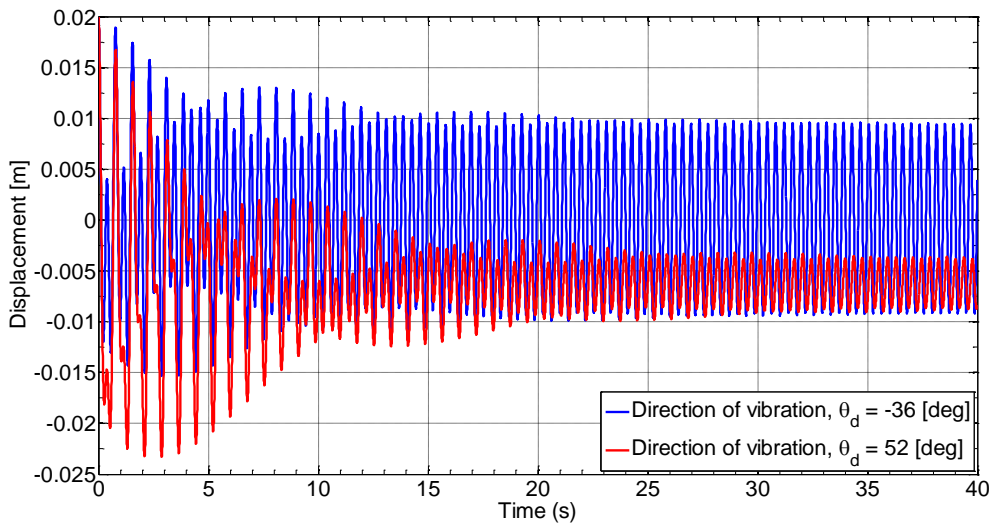


Figure 35 Lead-lag time response at 20° geometrical angle of attack

6. Summary

The work in this thesis, as part of the project in rebuilding the Red Wind Tunnel facility in DTU, was about designing a mount system for the airfoil model in the wind tunnel test section. Accordingly, after having reviewed literature on various mount systems design and construction, a mechanism was devised that allows three degree-of-freedom (DOF) motion such as pitching, plunging, and lead-lag. To this end, a 3D model of the mount system was prepared by using SOLIDWORKS software and documented in this thesis along with a description of its working principle. A case was taken to reinforce the motivations behind this thesis with time simulation of the governing equation and static airfoil data for the case in question. In this regard, Øye dynamic

stall model was implemented to show its effect in improving performance underestimation by using static data. An attempt was also made to show the effect of direction of vibration on aerodynamic damping. As a reference to future work this thesis was started with the idea to develop a panel code for the aerodynamic analysis of wing/tunnel interaction and even test the mount system in the wind tunnel, more appropriately in the new wind tunnel. For the flow simulation the viscous-inviscid flow solver Q³UIC which was developed and validated by Ramos García in DTU [22-23] can be implemented. Q³UIC is a quasi-3D viscous-inviscid interaction panel code flow analysis tool, based on the popular XFOIL airfoil design tool, for steady and unsteady flow which was implemented only for pitching motion, then extended to include aero-servo-elastic effects by Sirko Bartholomay. [24] However, the flow solver needs to be extended to include heaving and edgewise motions.

7. References

1. Farmer, M.G. *A Two-Degree-of-Freedom Mount System with Low Damping for Testing Rigid Wings at different Angles of Attack*, NASA TM-83302 (1982).
2. Yogesh Babbar; Vishvas Samuel Suryakumar; and Thomas W. Strganac *Experiments in Free and Forced Aeroelastic Response*, 51st AIAA Aerospace Sciences Meeting including the New Horizons Forum and Aerospace Exposition (2013).
3. De Marqui, C. Jr.; Rebolho D.C., Belo, E.M.; Marques, F.D.; and Tsunaki, R.H. *Design of an Experimental Flutter Mount System*, Journal of the Brazilian Society of Mechanical Sciences and Engineering XXIX (3):246–252 (2007).
4. Ko, J.; Strganac, T.W.; and Kurdila, A.J. *Adaptive Feedback Linearization for the Control Of a Typical Wing Section with Structural Nonlinearity*, Nonlinear Dynamics 18(3):289–301 (1999).
5. Waszak, M.R. *Modeling the Benchmark Active Control Technology Wind-Tunnel Model for Active Control Design Applications*, NASA TP-1998-206270 (1998).
6. Gjerek, B.; Drazumeric, R.; and Kosel, F.; *A Novel Experimental Setup for Multiparameter Aeroelastic Wind Tunnel Tests*, DOI: 10.1111/j.1747-1567.2012.00839.x (2012).
7. O'Neil, T. and Strganac *Nonlinear Aeroelastic Response - Analyses and Experiments*, Proceedings of the AIAA 34th Aerospace Sciences Meeting & Exhibit, AIAA Paper 96-0014 (1996).
8. Bir, G. and Jonkman, J. *Aeroelastic Instabilities of Large Offshore and Onshore Wind Turbines*, Journal of Physics: Conference Series 75 (2007) 012069.
9. Ricketts, R. *Experimental Aeroelasticity History, Status and Future in Brief*, NASA TM-102651(1990).
10. Ricketts, R.H. and Doggett, R.V. Jr. *Wind-Tunnel Experiments on Divergence of Forward Swept Wings*, NASA TP-1685 (1980).
11. Ruhlin, C.L.; Watson, J.J.; Ricketts, R.H.; and Doggett, R.V. Jr. *Evaluation of Four Subcritical Response Methods for On-Line Prediction of Flutter Onset in Wind Tunnel Tests*, AIAA Journal of Aircraft 20(10):835–840 (1983).
12. Foughner, J.T. Jr. and Bensinger, C.T. *F-16 flutter Model Studies with External Wing Stores*, NASA TM-74078 (1977).
13. Reed, W.H., III and Abbott F.T. Jr. *A New "Free-Flight" Mount System for High-Speed Wind-Tunnel Flutter Models*, NASA TM-X-50536 (1963).
14. Thompson, N. and Farmer, M. *Stability Analysis of an F/A-18 E/F Cable Mount Model*, NASA TM-108989 (1994).
15. Hansen, M.H. *Aeroelastic instability problems for wind turbines*; Wind Energy; 10:551–577; (2007).
16. McCroskey, W.J.; Carr, L.W. and McAlister, K.W. *Dynamic Stall Experiments on Oscillating Airfoils*, AIAA Journal, Vol.14, No. 1, pp. 57-63 (1976).

17. Luis Bernal; Michael Ol; Douglas Szczublewski; Craig Cox *Unsteady Force Measurements in Pitching-Plunging Airfoils*, 39th AIAA Fluid Dynamics Conference, 10.2514/6.2009-4031 (2009).
18. Øye, S. *Dynamic Stall, simulated as a time lag of separation*, in McAnulty (ed) Proc. 4th IEA Symposium on the Aerodynamics of Wind Turbines, ETSU-N-118, (1991).
19. Hansen, M.O.L. *Aerodynamics of Wind Turbines*, 2nd edition, Routledge, (2007).
20. Jeppe Johansen *Unsteady Airfoil Flows with Application to Aero-elastic Stability*, Risø National Laboratory, Roskilde, Denmark (October 1999).
21. Rasmussen F, Petersen JT, Madsen HAa. *Dynamic stall and aerodynamic damping*. ASME Journal of Solar Energy Engineering; 121: 150–155 (1999).
22. RAMOS-GARCIA, N.; SØRENSEN, J.N.; SHEN, W.Z.: *A quasi-3D viscous-inviscid interaction code: Q³UIC*. Journal of Physics, conference series. Making torque from wind (2012).
23. RAMOS-GARCÍA, Néstor: *Unsteady Viscous-Inviscid Interaction Technique for Wind Turbine Airfoils*, Technical University of Denmark, Phd. Thesis, 2011.
24. Sirko Bartholomay: *Implementation of aeroservoelastic effects into a two dimensional unsteady panel code and experimental validation*, Technical University of Denmark, Master. Thesis, 2013.
25. Petersen, J. T., Madsen, H. A., Enevoldsen, P., Ganander, H., Winkelaar, D. *Prediction of Dynamic Loads and Induced Vibrations in Stall*. Risø National Laboratory; Risø-R-1045 (EN), (May 1998).
26. Hansen, M.H. *Improved modal dynamics of wind turbines to avoid stall-induced vibrations*; Wind Energy; 6:179–195; (2003).
27. Hansen, M.H. *Aeroelastic eigenvalue analysis of three-bladed wind turbines*; 29th European Rotorcraft Forum; Friedrichshafen, Germany, (September 2003).

8. Appendix

8.1 Stiffness

Coordinate transformation from inertial reference frame (xy) to airfoil coordinate system ($x_{ew}y_{fw}$) to write system potential energy in terms of inertial reference frame coordinates.

$$\begin{Bmatrix} x_{ew} \\ y_{fw} \end{Bmatrix} = \begin{bmatrix} \cos\alpha_0 & \sin\alpha_0 \\ -\sin\alpha_0 & \cos\alpha_0 \end{bmatrix} \begin{Bmatrix} x \\ y \end{Bmatrix} = \begin{Bmatrix} x\cos\alpha_0 + y\sin\alpha_0 \\ -x\sin\alpha_0 + y\cos\alpha_0 \end{Bmatrix}$$

When the direction of vibration is at an angle θ_d from the rotor plane, the rotation angle α_0 in the above transformation is replaced by $\alpha_0 + \theta_d$.

System kinetic energy,

$$U = \frac{1}{2}k_{ew}x_{ew}^2 + \frac{1}{2}k_{fw}y_{fw}^2 + \frac{1}{2}k_{\theta}\theta^2$$

$$U = \frac{1}{2}k_{ew}(x^2\cos^2\alpha_0 + xysin2\alpha_0 + y^2\sin^2\alpha_0) + \frac{1}{2}k_{fw}(y^2\cos^2\alpha_0 - xysin2\alpha_0 + x^2\sin^2\alpha_0) + \frac{1}{2}k_{\theta}\theta^2$$

Lagrange's equation

$$\begin{aligned}
& -\frac{d}{dt}\left(\frac{\partial(T-U)}{\partial\dot{x}}\right) + \frac{\partial(T-U)}{\partial x} - \frac{\partial D}{\partial\dot{x}} + F_x = 0 \\
\Rightarrow & -\frac{d}{dt}(m\dot{x}) - (k_{ew}\cos^2\alpha_0 + k_{fw}\sin^2\alpha_0)x - \frac{1}{2}(k_{ew}\sin 2\alpha_0 - k_{fw}\sin 2\alpha_0)y - c_x\dot{x} + F_x = 0 \\
& -\frac{d}{dt}\left(\frac{\partial(T-U)}{\partial\dot{y}}\right) + \frac{\partial(T-U)}{\partial y} - \frac{\partial D}{\partial\dot{y}} + F_y = 0 \\
\Rightarrow & -\frac{d}{dt}(m\dot{y} - mr_{cg}\dot{\theta}) - (k_{fw}\cos^2\alpha_0 + k_{ew}\sin^2\alpha_0)y - \frac{1}{2}(k_{ew}\sin 2\alpha_0 - k_{fw}\sin 2\alpha_0)x - c_y\dot{y} + F_y \\
& = 0 \\
& -\frac{d}{dt}\left(\frac{\partial(T-U)}{\partial\dot{\theta}}\right) + \frac{\partial(T-U)}{\partial\theta} - \frac{\partial D}{\partial\dot{\theta}} + M_{ea} = 0 \\
\Rightarrow & -\frac{d}{dt}(mr_{cg}\dot{y} + I_{ea}\dot{\theta}) - k_\theta\theta - c_\theta\dot{\theta} + M_{ea} = 0
\end{aligned}$$

In matrix form

$$\begin{aligned}
\underbrace{\begin{bmatrix} m & 0 & 0 \\ 0 & m & -mr_{cg} \\ 0 & -mr_{cg} & I_{ea} \end{bmatrix}}_M \underbrace{\begin{Bmatrix} \ddot{x} \\ \ddot{y} \\ \ddot{\theta} \end{Bmatrix}}_{\dot{q}} + \underbrace{\begin{bmatrix} c_x & 0 & 0 \\ 0 & c_y & 0 \\ 0 & 0 & c_\theta \end{bmatrix}}_C \underbrace{\begin{Bmatrix} \dot{x} \\ \dot{y} \\ \dot{\theta} \end{Bmatrix}}_{\dot{q}} \\
+ \underbrace{\begin{bmatrix} k_{ew}\cos^2\alpha_0 + k_{fw}\sin^2\alpha_0 & \frac{1}{2}(k_{ew}\sin 2\alpha_0 - k_{fw}\sin 2\alpha_0) & 0 \\ \frac{1}{2}(k_{ew}\sin 2\alpha_0 - k_{fw}\sin 2\alpha_0) & k_{fw}\cos^2\alpha_0 + k_{ew}\sin^2\alpha_0 & 0 \\ 0 & 0 & k_\theta \end{bmatrix}}_K \underbrace{\begin{Bmatrix} x \\ y \\ \theta \end{Bmatrix}}_q = \underbrace{\begin{Bmatrix} F_x \\ F_y \\ M_{ea} \end{Bmatrix}}_F
\end{aligned}$$

Or in compact form the equation of motion can be written as $M\ddot{q} + C\dot{q} + Kq = F(t)$.

8.2 Aerodynamic damping

Referring to **Figure 32**, the aerodynamic force in the direction of vibration is

$$F_x = 1/2\rho V_{rel}^2 A [C_l(\alpha) \sin(\phi - \theta_d) - C_d(\alpha) \cos(\phi - \theta_d)]$$

Linearizing this force using Taylor expansion about $\dot{x} = 0$ (Cf. appendix), as shown by *M. H. Hansen*, considering only the lead-lag motion (x - direction), and the steady-state values inflow angle ϕ_0 , relative inflow speed $V_{rel,0}$, and angle of attack α_0 , at $\dot{x} = 0$

$$\begin{aligned}
\tan\phi &= \frac{V_{rel,0}\sin\phi_0 + \dot{x}\sin\theta_d}{V_{rel,0}\cos\phi_0 + \dot{x}\cos\theta_d} \\
\alpha &= \phi + \alpha_g \\
V_{rel}^2 &= (V_{rel,0}\cos\phi_0 + \dot{x}\cos\theta_d)^2 + (V_{rel,0}\sin\phi_0 + \dot{x}\sin\theta_d)^2 \\
F_x &= F_x(0) + \left.\frac{\partial F_x}{\partial\dot{x}}\right|_{\dot{x}=0} \dot{x} \\
F_x(0) &= 1/2\rho V_{rel,0}^2 A [C_l(\alpha_0) \sin(\phi_0 - \theta_d) - C_d(\alpha_0) \cos(\phi_0 - \theta_d)]
\end{aligned}$$

$$\begin{aligned}\frac{\partial F_x}{\partial \dot{x}} &= 1/2\rho A \left\{ [2\dot{x} + 2V_{rel,0} \cos(\theta_d - \phi)] [C_l \sin(\phi - \theta_d) - C_d \cos(\phi - \theta_d)] \right. \\ &\quad + \left[\frac{dC_l}{d\alpha} \frac{\partial \alpha}{\partial \dot{x}} \sin(\phi - \theta_d) + \cos(\phi - \theta_d) \frac{\partial \phi}{\partial \dot{x}} C_l - \frac{dC_d}{d\alpha} \frac{\partial \alpha}{\partial \dot{x}} \cos(\phi - \theta_d) \right. \\ &\quad \left. \left. + \sin(\phi - \theta_d) \frac{\partial \phi}{\partial \dot{x}} C_d \right] [V_{rel}^2 + \dot{x}^2 + 2V_{rel,0} \dot{x} \cos(\theta_d - \phi)] \right\}\end{aligned}$$

Here,

$$\begin{aligned}\phi &= \tan^{-1} \left[\frac{V_{rel,0} \sin \phi_0 + \dot{x} \sin \theta_d}{V_{rel,0} \cos \phi_0 + \dot{x} \cos \theta_d} \right] \\ \Rightarrow \frac{\partial \phi}{\partial \dot{x}} \Big|_{\dot{x}=0} &= \frac{\partial \alpha}{\partial \dot{x}} \Big|_{\dot{x}=0} = \frac{\sin(\theta_d - \phi_0)}{V_{rel,0}}\end{aligned}$$

$$\begin{aligned}\frac{\partial F_x}{\partial \dot{x}} \Big|_{\dot{x}=0} &= 1/2\rho AV_{rel,0} \left\{ [2 \cos(\theta_d - \phi_0)] [C_l \sin(\phi_0 - \theta_d) - C_d \cos(\phi_0 - \theta_d)] \right. \\ &\quad + \left[-C_l' \sin^2(\theta_d - \phi_0) + \frac{1}{2} C_l \sin(2\theta_d - 2\phi_0) - \frac{1}{2} C_d' \sin(2\theta_d - 2\phi_0) \right. \\ &\quad \left. \left. - C_d \sin^2(\theta_d - \phi_0) \right] \right\} \\ &= 1/2\rho AV_{rel,0} \left\{ -C_l \sin(2\theta_d - 2\phi_0) - C_d [1 + \cos(2\theta_d - 2\phi_0)] - \frac{1}{2} C_l' [1 - \cos(2\theta_d - 2\phi_0)] \right. \\ &\quad \left. + \frac{1}{2} C_l \sin(2\theta_d - 2\phi_0) - \frac{1}{2} C_d' \sin(2\theta_d - 2\phi_0) - \frac{1}{2} C_d [1 - \cos(2\theta_d - 2\phi_0)] \right\} \\ &= -1/2\rho AV_{rel,0} \left\{ \frac{1}{2} C_l \sin(2\theta_d - 2\phi_0) + \frac{1}{2} C_d [3 + \cos(2\theta_d - 2\phi_0)] + \frac{1}{2} C_l' [1 - \cos(2\theta_d - 2\phi_0)] \right. \\ &\quad \left. + \frac{1}{2} C_d' \sin(2\theta_d - 2\phi_0) \right\} \\ \frac{\partial F_x}{\partial \dot{x}} \Big|_{\dot{x}=0} &= -\eta = -\frac{1}{4} \rho AV_{rel,0} \left\{ C_d [3 + \cos(2\theta_d - 2\phi_0)] + C_l' [1 - \cos(2\theta_d - 2\phi_0)] + (C_l \right. \\ &\quad \left. + C_d') \sin(2\theta_d - 2\phi_0) \right\}\end{aligned}$$

$$\eta = \frac{1}{4} \rho AV_{rel,0} [C_d (3 + \cos(2\theta_d - 2\phi_0)) + C_l' (1 - \cos(2\theta_d - 2\phi_0)) + (C_l + C_d') \sin(2\theta_d - 2\phi_0)]$$

8.3 Different views of the mount system

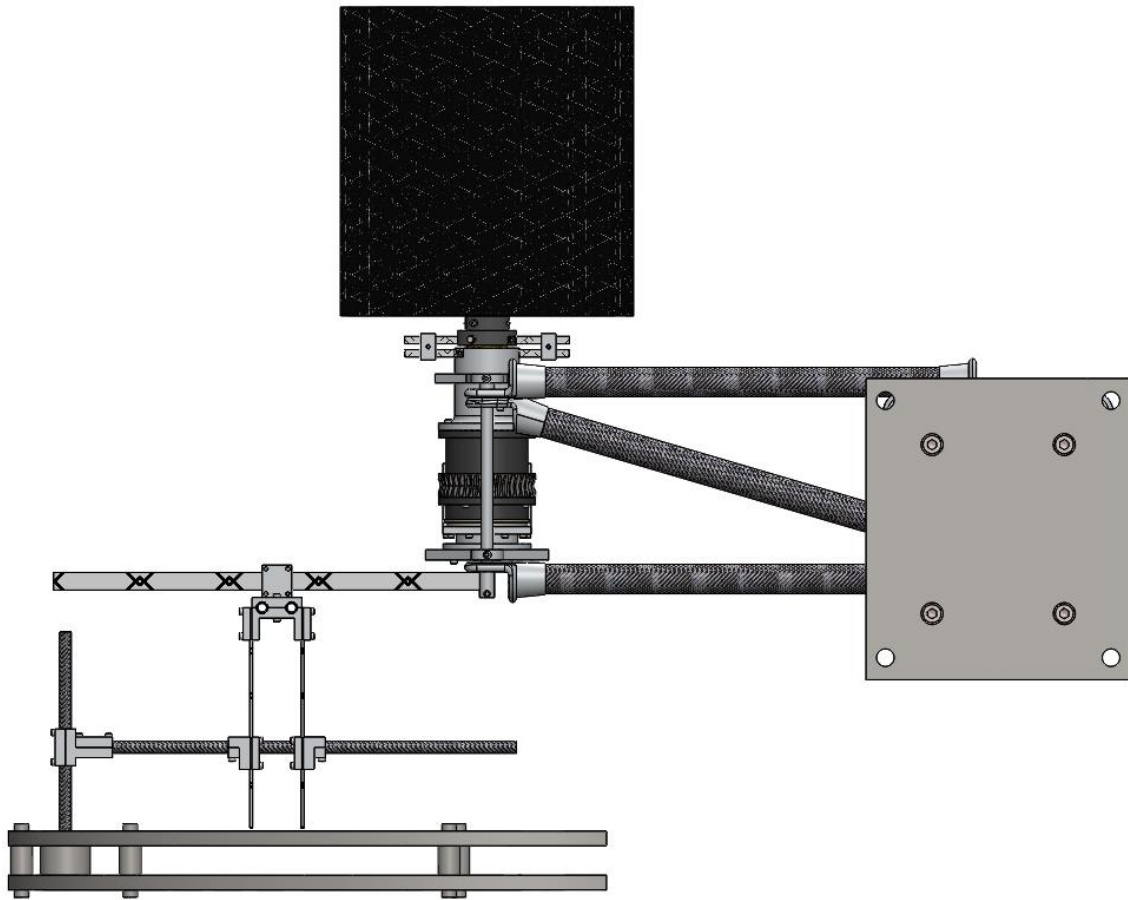


Figure 36 Left side view of the mount system

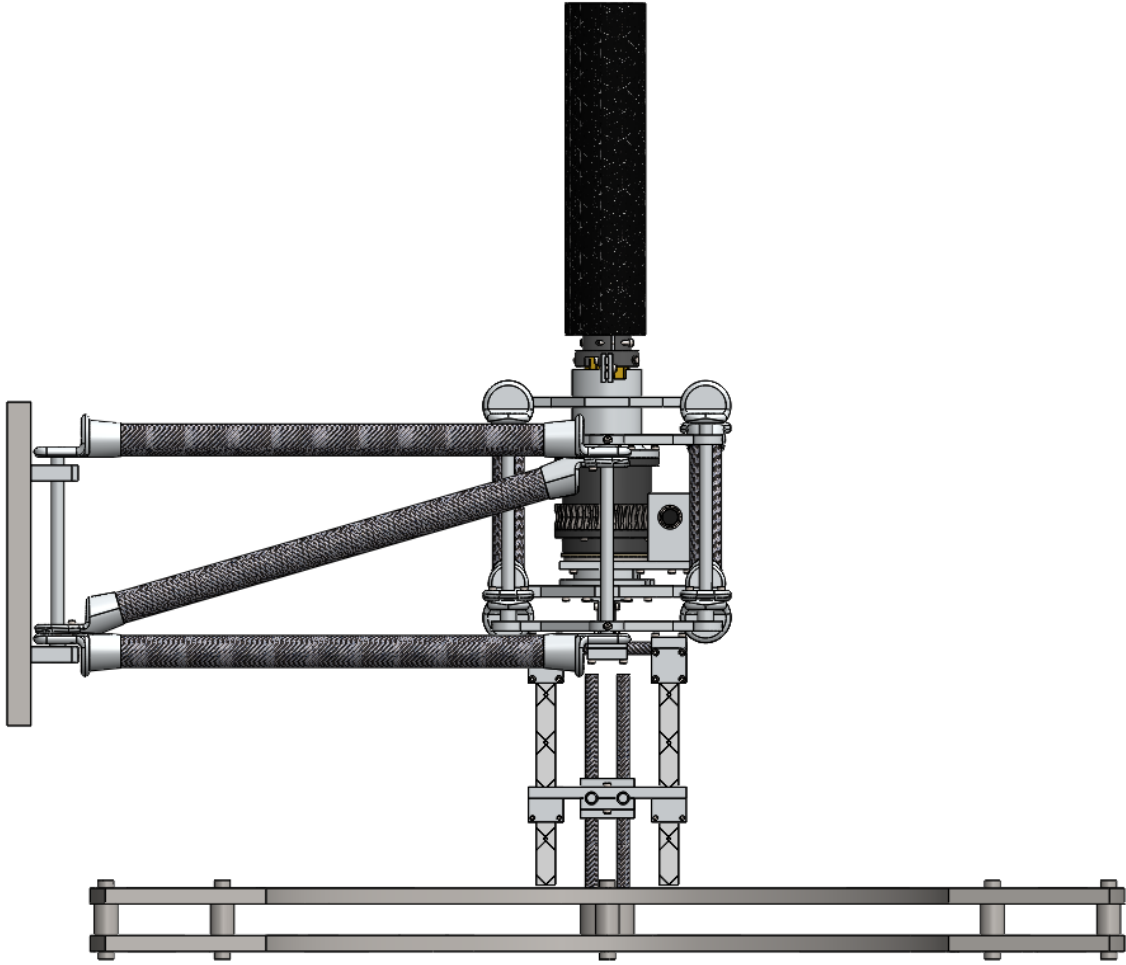


Figure 37 Front view of the mount system

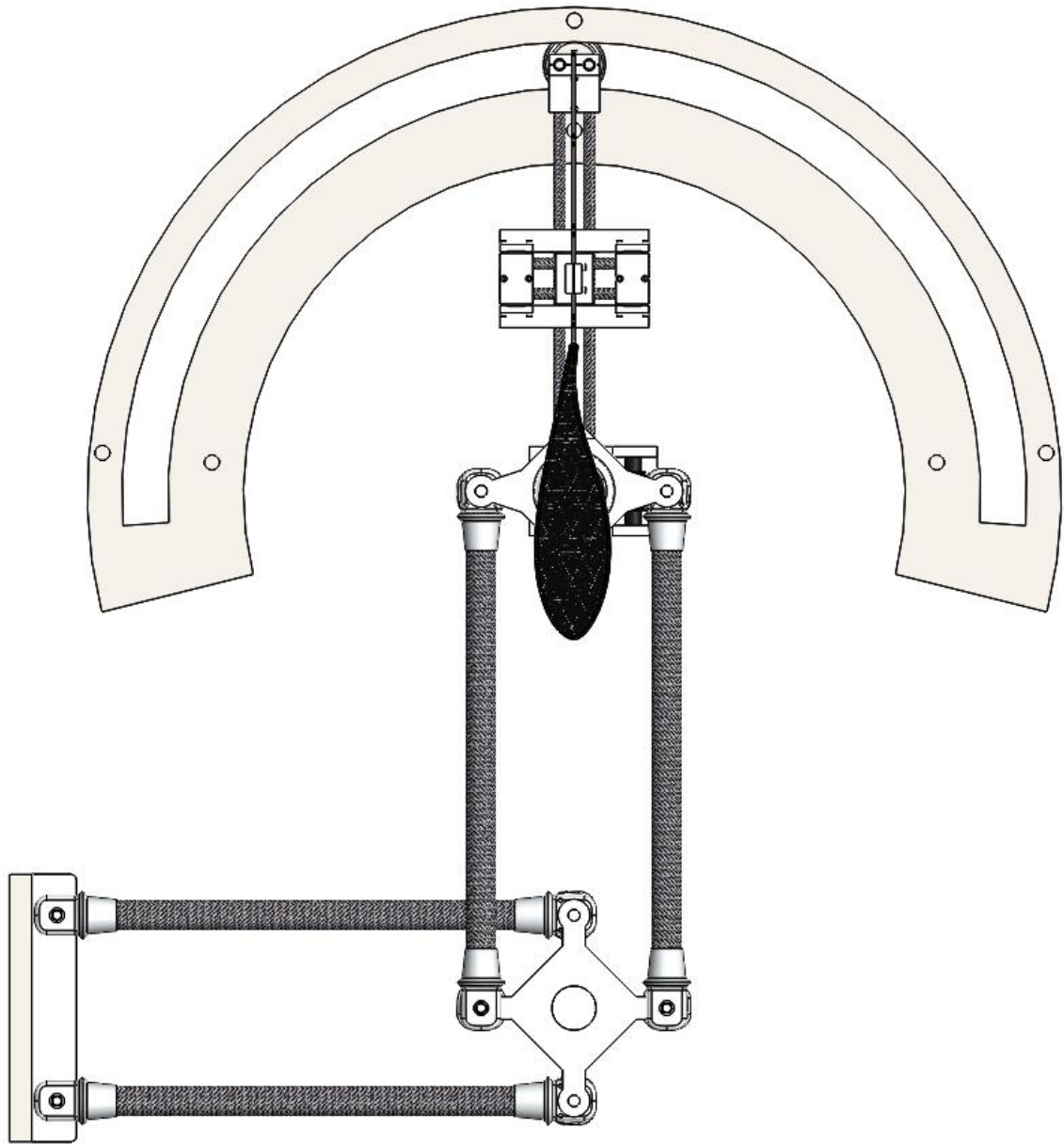


Figure 38 Back view of the mount system

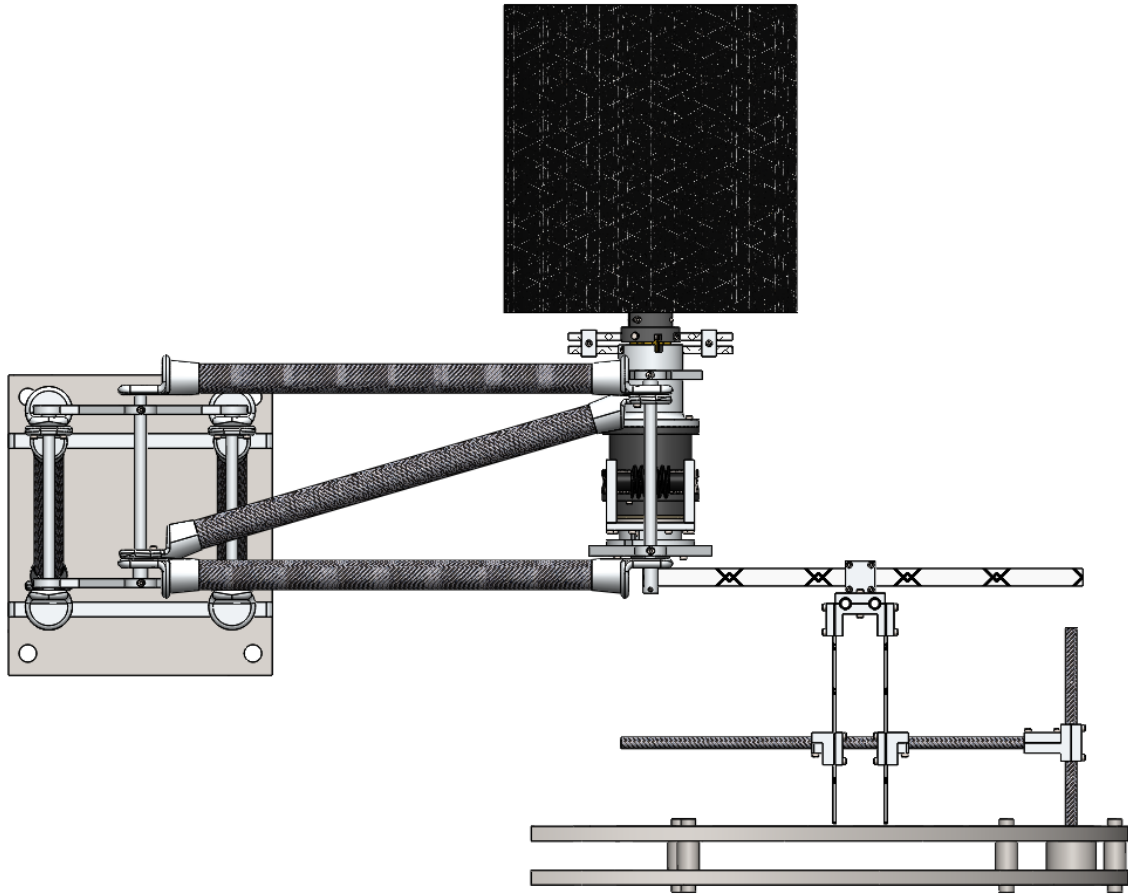


Figure 39 Right side view of the mount system

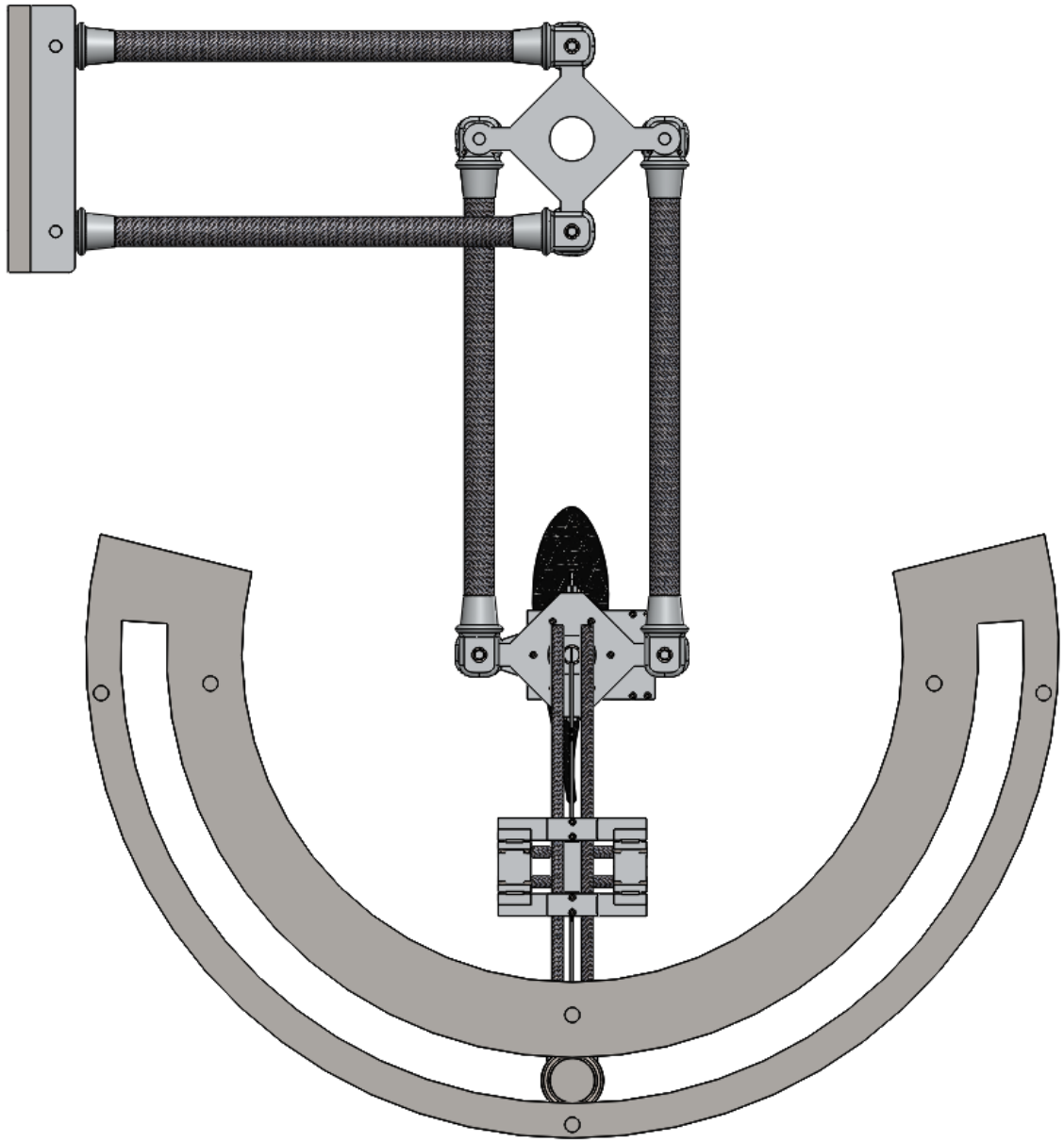


Figure 40 Bottom view of the mount system

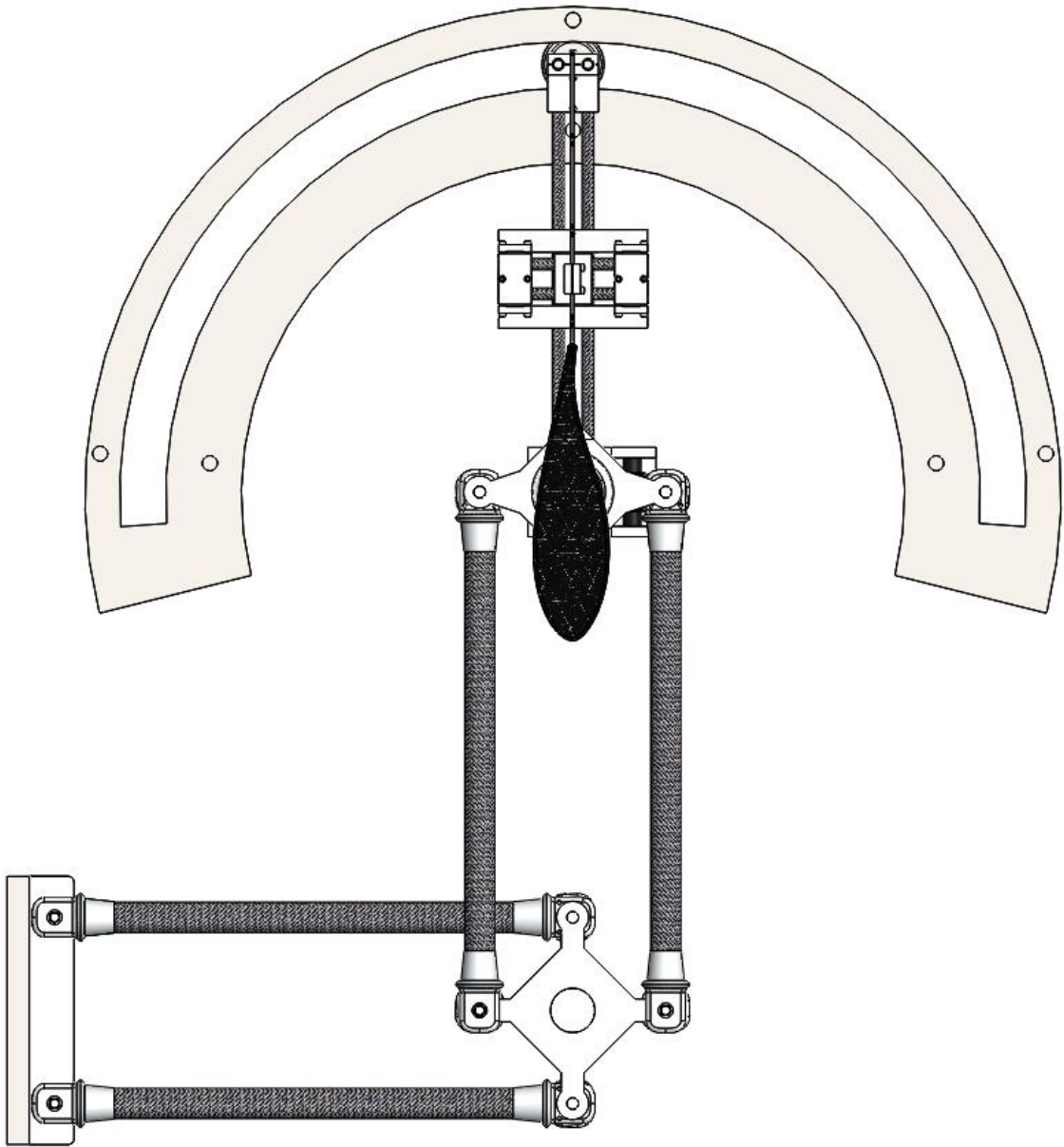


Figure 41 Top view of the mount system

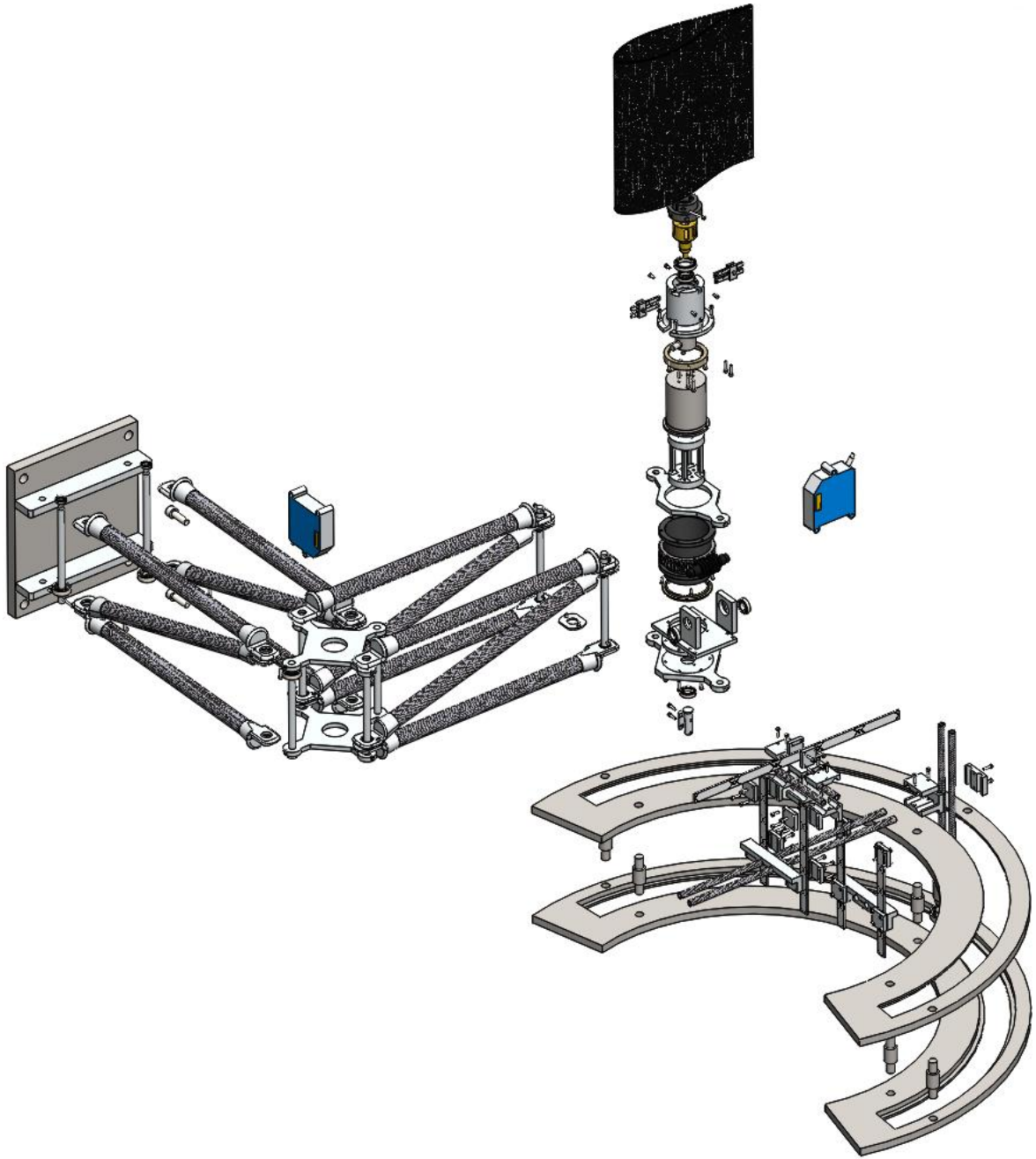


Figure 42 Exploded view of the mount system

8.4 Masses of parts

S.N	Parts	Material	Count	Mass of single part [Grams]
1	Carbon tubes	Carbon fiber	8	17.91
2	Carbon tube fixture1	Aluminium	8	9.06
3	Carbon tube fixture2	Aluminium	8	10.26
4	Stiffener carbon tubes	Carbon fiber	4	18.91
5	Stiffener tube fixture	Aluminium	8	7.06
6	Base attachment	Steel	1	539.35
7	Pivot joint 1 fixture	Aluminium	2	50.92
8	Pivot joint 1 shaft	Aluminium	2	6.71
9	Pivot joint 2 fixture	Aluminium	2	34.95
10	Pivot joint 2 shaft 1	Aluminium	2	6.45
11	Pivot joint 2 shaft 2	Aluminium	2	6.88
12	Pivot joint 3 fixture	Aluminium	2	18.66
13	Pivot joint 3 shaft	Aluminium	2	6.64
14	Radial ball bearing, SKF - 608 - 8,SI,NC,8_68	Steel	8	1.89
15	Radial ball bearing, SKF - 618-6 - 10,SI,NC,10_68	Steel	8	0.3
16	Radial ball bearing, SKF - 61801 - 14,SI,NC,14_68	Steel	1	0.93
17	Radial ball bearing, SKF - 61803 - 20,SI,NC,20_68	Steel	1	1.21
18	Worm gear	POM	1	20.17
19	Radial ball bearing, SKF - 61800 - 14,SI,NC,14_68	Steel	3	0.82
20	Worm wheel fixture	POM	1	29.80
21	Interface between pitch motion sensor and body	Steel	1	20.59
22	Pitch motion sensor	AL7075	1	27.03
23	Teflon bearing 1	Teflon	1	3.45
24	Teflon bearing 2	Teflon	1	2.61
25	Pitch motion encoder fixture	Aluminium	1	44.90
26	SCH24 encoder for pitch motion	-	1	8.70
27	Pitch motion shaft	Brass	1	9.50
28	Model fixture	POM	1	8.76
29	Pitch motion sensor bottom support	Aluminium	1	15.93
30	Pitch motion support plate	Aluminium	1	17.84
31	Worm support	Aluminium	2	7.00
32	Flapwise spring fixture	Aluminium	2	1.55
33	Torsional spring fixture	Aluminium	4	0.45
34	Torsional spring	Steel or carbon fibre	4	0.41 (carbon fiber)

Table 3 Partial part list of the mount system

9. Acknowledgements

I would like to extend my sincere gratitude to my supervisors Robert Mikkelsen and Martin O. L. Hansen for their invaluable support during the thesis work and making me feel alive every time I meet them. I would also like to thank Néstor Ramos García for his kind support related to his flow analysis tool known as Q³UIC. In fact I am also indebted to my friends Yifei He and Ashok Kumar Nedumaran for keeping in touch and help me to get into gear during bad times. Last, but obviously not least, my deepest gratitude and great appreciation goes to my wife as it would have been impossible for me to get here without her love and inspiration. Above all, I wish to thank the Almighty God for holding me up and giving me the strength to finalize my study.

DTU Wind Energy is a department of the Technical University of Denmark with a unique integration of research, education, innovation and public/private sector consulting in the field of wind energy. Our activities develop new opportunities and technology for the global and Danish exploitation of wind energy. Research focuses on key technical-scientific fields, which are central for the development, innovation and use of wind energy and provides the basis for advanced education at the education.

We have more than 240 staff members of which approximately 60 are PhD students. Research is conducted within nine research programmes organized into three main topics: Wind energy systems, Wind turbine technology and Basics for wind energy.

Danmarks Tekniske Universitet

DTU Vindenergi
Nils Koppels Allé
Bygning 403
2800 Kgs. Lyngby
Phone 45 25 25 25

info@vindenergi.dtu.dk
www.vindenergi.dtu.dk

Delft University of Technology

Faculty of Aerospace Engineering,
TU Delft
Kluyverweg 1, 2629 HS Delft
the Netherlands
hone +31 15 2786388

study-ae@tudelft.nl
www.lr.tudelft.nl